Aerodynamic Shape Optimization for Dynamic Stall Mitigation in Floating Vertical Axis Wind Turbine Blades

Qiang Zhang [a,b], Musa Bashir [c], Sean Malkeson [b], Qingsong Liu [c], Chun Li [a *], Weipao Miao [a,c], Wanfu Zhang [a], Minnan Yue [a], Zifei Xu [c], Jin Wang [b *]

a. School of Energy and Power Engineering, University of Shanghai for Science and Technology, Shanghai, 200093. China

b. Liverpool Logistics, Offshore and Marine (LOOM) Research Institute, Liverpool John Moores University, Liverpool, Byrom Street, L3 3AF, UK

c. Department of Civil and Environmental Engineering, University of Liverpool, Liverpool, L69 3BX, UK

Abstract: Conventional aerodynamic shape optimization (ASO) approaches typical rely on thousands of high-fidelity computational fluid dynamics (CFD) simulations, making the process computationally prohibitive for practical applications. To address such a limitation, this study develops a data-driven ASO framework employing surrogate-based optimization (SBO) to efficiently map blade geometric parameters to aerodynamic forces. The methodology involves: (1) constructing an initial surrogate model with 200 samples, (2) successive refinement through 60 infill samples using the Expected Improvement (EI) criterion, and (3) validation via normalized root mean square error (NRMSE). Global optimization is subsequently performed using genetic algorithms. The optimized airfoil exhibits a streamlined leading-edge profile with increased thickness and reduced leading-edge radius compared to the baseline. Results indicate that optimized blade exhibits significant reductions in drag and moment coefficients, respectively, during DPM cycles. The increase of tangential force coefficient indicates the suppression of negative torque, resulting in a more stable torque output from the blade. By mitigating dynamic stall effects and enhancing torque stability, the proposed optimization strategy provides a viable pathway to improving the efficiency and reliability of floating VAWT blade, thereby supporting their broader deployment in offshore environments.

Keywords: Aerodynamic shape optimization; Vertical axis wind turbine; Darrieus-type pitching motion; Data-driven; Gaussian process regression; Dynamic stall characteristic.

Nomenclature

2D	Two-dimensional	α	Angle of Attack
3D	Three-dimensional	σ	Rotor solidity
AoA	Angle of Attack	λ	Tip Speed Ratio
ASO	Aerodynamic shape optimization	ω	Rotor rotate speed
CFD	Computational Fluid Dynamics	R	Rotor radius
DPM	Darrieus- type Pitching Motion	V_∞	Incoming wind velocity
NRMSE	Normalized Root Mean Square Error	Vr	Relative velocity
TSR	Tip Speed Ratio	F_L	Lift force
GPR	Gaussian Process Regression	F_D	Drag force
LHS	Latin Hypercube Sample	F_n	Normal force
URANS	Unsteady Reynolds Averaged Navier Stokes	F_t	Tangential force
EI	Expected Improvement	C_T	Torque coefficient
GA	Genetic Algorithm	C_p	Power coefficient
SBO	Surrogate-Based Optimization	T	Torque

* Corresponding author: Prof. Chun Li. E-mail address: lichun@usst.edu.cn.

UDF	User-Defined Function	Re	Reynolds number
ρ	Air density	C_l	Lift coefficient
D	Sample sets	C_d	Drag coefficient
$\boldsymbol{x}$	Vector of design variables	C_m	Moment coefficient
$\boldsymbol{y}$	Response value	C_n	Coefficient of normal force
$\hat{\boldsymbol{y}}$	GPR prediction result	C_t	Coefficient of tangential force
x_c	Dimensionless chordwise position	θ	Azimuth angle
y_s	The y coordinates of upper and lower surface	t	Physical time
n	Number of design variables	T	Time of one rotation of the blade
n_s	Number of samples	$\boldsymbol{\theta}$	Vector of kriging hyperparameters
n_t	Test set samples	$\boldsymbol{\beta}$	Regression coefficient
N	Number of instantaneous AoA per pitching cycle	X_u	Unknown point in the design space
c	Airfoil chord length	$\hat{Y}$	Mean of unknown point
R_{LE}	Leading edge radius	$\hat{s}^2$	Mean square error of unknown point
$T_{\max}$	Airfoil maximum thickness	R^2	R-squared
Δy_{te}	Airfoil trailing edge thickness	Δy	The difference in vertical coordinates
C	Covariance matrix	y^+	Non-dimensionalized first layer grid height

1. Introduction

Wind energy, as a sustainable, clean, and renewable energy source, has the advantages of abundant reserves and great potential for development, attracting widespread attention from governments and energy organizations [1, 2, 3]. According to a report by the Global Wind Energy Council (GWEC), global wind power installations reached 117 GW in 2024, bringing the total installed wind power capacity worldwide to 1,136 GW [4]. Offshore wind power will increase from 16 GW in 2025 to 34 GW in 2030, pointing to a prosperous future for offshore wind power. Horizontal-axis wind turbines (HAWTs) and vertical-axis wind turbines (VAWTs) are the two main types of large-scale equipment used to convert wind energy into electricity [5]. Over the past 30 years, since HAWTs have a higher wind energy utilization rate, researchers have primarily focused on the development and commercialization of HAWTs, and have developed large wind turbines exceeding 20 MW [6]. Meanwhile, VAWTs remain at the theoretical conceptual design stage, or are applied to small-scale products for urban landscapes [7, 8].

In recent years, wind turbines have been increasingly installed at sea to utilize high-quality offshore wind resources. However, this growth has been constrained by the high cost of energy of HAWT installations, particularly for traditional fixed platforms [9, 10]. Therefore, VAWTs have attracted attention once again due to their beneficial design characteristics (low center of gravity and insensitivity to wind direction), which enhance their adaptability to offshore floating conditions. Additionally, compared to HAWTs, VAWTs have simpler manufacturing processes, lower installation and maintenance costs, and are easier to scale up. This significantly reduces the high cost of investment in offshore wind energy utilization and enables VAWTs to have a lower COE during power generation [11-12]. These advantages of VAWTs are considered to be more promising than HAWTs for offshore wind energy utilization.

Although the development of VAWTs has many advantages, the relatively low rotor power coefficient is the most significant challenge that limits its application [13]. At this stage, there are three categories of methods to improve the power coefficient of VAWTs:

a) Adjust operating parameters

The operating parameters of VAWTs include the number of blades, tip speed ratio, pitch angle, rotor distance, etc. In addition to adjusting the number of blades and tip speed ratio to the optimal configuration to improve the power coefficient of VAWTs. A typical method for adjusting VAWT operating parameters is via pitch angle control. This technology uses blade pitch to achieve dynamic angle of attack control, effectively suppressing flow separation. Gupta et al. [14] applied active blade pitch technology to mitigate flow separation at different Reynolds numbers and tip speed ratios. The results showed that the power coefficient of a small VAWT reached 0.44 at a tip speed ratio of 1.5. Li et al. [15] combined numerical simulation and genetic algorithm to optimize the blade pitch angle, resulting in a maximum increase in power coefficient by 0.317 for the VAWT. In addition, contra-rotating VAWTs by adjusting the distance between them are also considered a good solution due to the advantages of balanced power and stability. Radhakrishnan et al. [16] used orthogonal design to analyze the four parameters of the blades and the results showed that suitable rotor distance achieved 14% increase in the power coefficient of contra-rotating VAWTs, which is a better application prospect compared to single VAWTs.

b) Local modification of airfoil shape and additional devices

The purpose of modifying the local shape of the airfoil is to change the boundary layer fluid flow state in order to improve the aerodynamic performance of the VAWT. For example, Wang et al. [17] applied wave serrations to the leading edge and increased the power of the modified VAWT by 18.3% compared to the baseline airfoil. Sobhani et al. [18] simulated a dimpled airfoil on VAWT and analyzed different dimple diameters and positions, and found that when the dimple is located at the leading edge of the pressure side, the power is increased by 25%. Bhavsar et al. [19] studied the effect of slots on the DU-99-W-405 airfoil over a wide range of angles of attack, achieving a lift-to-drag ratio improvement of 116% compared to the reference airfoil. Additional devices are also used as a way of changing the flow state on the airfoil surface, usually by installing devices near the airfoil or VAWT rotor. The devices for the airfoil include gurney flap [20], trailing edge flap [21], synthetic jet [22], leading edge suction [23], and winglet [24]. Using the entire VAWT rotor as the object, the guide vane [25] and deflection plate [26] improve aerodynamic performance by increasing the inflow wind speed.

c) To develop dedicated airfoils for VAWTs

The blades are the key components of a VAWT for capturing wind energy, and their airfoil shape determines aerodynamic efficiency. Currently, most VAWT airfoils are derived from aerospace and HAWT airfoils [29, 30]. However, the characteristic of periodic continuous changes in the angle of attack for VAWT blades results in a more complex flow field. This leads to the blades frequently operating in a dynamic stall state, thereby resulting in significant fluctuations in aerodynamic loads. Therefore, it is necessary to design dedicated airfoils that are adapted to the operating environment of VAWTs to mitigate dynamic stall and improve wind energy utilization. Aerodynamic shape optimization (ASO) is an effective method to enhance the airfoil's performance. For example, in the case of a wide range of angles of attack during VAWT rotation, Wang et al. [31] considered multiple angles of attack in the optimization and used the tangential force coefficients as the objective function. When the optimized airfoil was applied to the VAWT, an 8.45% increase in the power coefficient was achieved compared to the prototype. Furthermore, since VAWT is particularly sensitive to dynamic stall, there is an urgent needed to improve its aerodynamic stability. Zhang et al. [32] used the average power coefficient of VAWT and the coefficient of variation of shaft as optimization objectives, using a multi-objective genetic algorithm to obtain the optimized airfoil. The results showed that the optimized blade effectively suppressed the flow separation at different azimuths.

Although additional devices can improve aerodynamic performance, they can often require complex control systems to achieve significant effects. This active/passive control method is not economical for the large-scale application of VAWT. In contrast, developing dedicated airfoils for VAWTs does not increase manufacturing complexity or costs, therefore can be regarded as a more feasible option. Therefore, this paper proposes a VAWT blade optimization method by combining high-precision computational fluid dynamics (CFD) method and surrogate based optimization (SBO) techniques. Considering the dynamic stall phenomenon during blade rotation, and with the objectives of reducing the load fluctuation and improving the aerodynamic performance and stability, an airfoil with better comprehensive performance is obtained in this study.

1.1 Review of VAWT blade optimization

ASO is a primary objective in mechanical design, aiming to improve aerodynamics performance during the design phase. The concept of ASO was first proposed by Hicks et al. [33] in the optimization of aircraft airfoil shapes for drag reduction. Subsequently, ASO has undergone significant development within fluid dynamics, with applications in aircraft [34], helicopters [35], automobiles [36], wind turbines [39, 40], and compressors [41]. Dynamic stall, an aerodynamic instability phenomenon caused arising from variations in the airfoil's angle of attack, compromises both efficiency and structural strength. To address this, ASO has been employed to suppress or delay dynamic stall, thereby reducing load fluctuations and enhancing overall aerodynamic performance.

ASO requires multiple computations of the target (aerodynamic forces) to achieve optimal geometry, making the computational cost of each CFD model as a critical factor in optimization efficiency. For VAWTs, aerodynamic forces have traditionally been estimated using the Multiple Streamtube (MST) model, which divides the actuator disk into multiple individual streamtubes. The momentum across the rotor is then computed based on velocity variations within each streamtube combined with the Bernoulli equation. While this approach offers rapid solution times, its computational accuracy is inherently limited.

Examples of VAWT airfoil ASO applications based on the Multiple Streamtube model include the following. Liang et al. [42] employed the MST model to obtain aerodynamic forces for a VAWT and developed a Genetic Algorithm (GA)-based optimization framework, where the optimized NACA0015 airfoil achieved an 8.87% increase in tangential force coefficient. Sanaye et al. [43] applied an improved Double Multiple Streamtube (DMST) model for VAWT aerodynamic modeling, with the optimized configuration reaching a maximum power coefficient of 0.49. Zhao et al. [44] formulated the minimization of two negative torque azimuth angles, calculated via the DMST method, as optimization objectives, resulting in a 6% enhancement of the maximum power coefficient. Chern et al. [45] integrated the direct-forcing Immersed Boundary Method (IBM) with a GA to optimize an airfoil, achieving a 5.61% improvement in the tangential force coefficient during VAWT rotor rotation.

In recent years, rapid advancements in computational performance have enabled the use of high-fidelity CFD models. Accurate aerodynamic simulations now facilitate the acquisition of superior geometric configurations. However, during optimization searches within the design space, the optimization cost remains challenging if aerodynamic forces are computed using CFD for each evaluation, as it typically involves thousands of CFD simulations, particularly for three-dimensional models. Consequently, Surrogate-Based Optimization (SBO) has been developed to reduce computational expense and enhance optimization efficiency. The general SBO workflow consists of four steps: (1) Selection of sample points within the design space. (2) Computation of aerodynamic responses at these sample points using high-fidelity CFD. (3) construction of a surrogate model that maps geometric parameters to aerodynamic responses, enabling evaluation in place of costly CFD simulations, and (4) application of an optimization algorithm to the surrogate model in order to identify the optimal geometry.

Common surrogate models in engineering applications include: Response Surface Methodology (RSM), Kriging models, Artificial Neural Networks (ANN), Radial Basis Functions (RBF), Support Vector Regression (SVR), and Gaussian Process Regression (GPR), among others. Several studies have applied SBO for ASO in VAWT performance improvement. Chen et al. [46] combined RSM with a Genetic Algorithm to optimize thickness and camber distributions of VAWT airfoils. Sanaye et al. [47] employed an ANN to construct functional relationships between airfoil parameters (chord length, pitch angle) and the power coefficient, significantly reducing computational time compared to 3D CFD simulations. Cardoso et al. [48] compared the prediction accuracy of RSM, ANN, and Kriging models for VAWT aerodynamic data, showing that ANN and Kriging models are more suitability for fitting nonlinear data, with the Kriging-based optimization model increasing the power coefficient by 7.92%. Wang et al. [49] developed a Kriging-based optimization methodology integrated with a Genetic Algorithm, achieving a 14.2% enhancement of the VAWT rotor's power coefficient. Cheng et al. [50] constructed multiple surrogate models, including ANN, SVR, GPR and decision tree regression (DTR) to solve the problem of low efficiency of VAWT numerical simulation. Their results showed that SVR and GPR provided the best prediction ability, with R^2 exceeding 0.99. Dorosti et al. [51] implemented direct optimization and GPR-based SBO framework and reported that integrating surrogate models into the optimization workflow reduced computational costs by 78%.

1.2 Innovation of current research

Traditional studies of airfoil dynamic stall have predominantly employed sinusoidal pitching motions, leveraging their periodic similarity to characterize fundamental dynamic stall behavior [52]. However, while sinusoidal oscillations ensure periodicity, their angle of attack variations differ substantially from actual blade kinematics in VAWTs, as analyzed in Section 3.1. In Darrieus-type VAWTs, blade motion follows a more complex pitching regime, herein termed Darrieus-type Pitching Motion (DPM). Consequently, this study adopts DPM rather than conventional sinusoidal motion to investigate dynamic stall under operationally relevant VAWT conditions. Furthermore, few studies have treated individual airfoils as fundamental elements for VAWT performance analysis and optimization. Compared with full three-blade rotor studies, our DPM-focused approach using Surrogate-Based Aerodynamic Shape Optimization (SBO-ASO) significantly reduces computational costs while maintaining physical fidelity.

Building on these challenges, this work presents a detailed analysis of the dynamic stall mechanism of DPM of VAWT blades, and applies ASO to improve stall characteristics. The primary innovations and contributions of this study are as follows:

(1) A pioneering investigation of VAWT blade dynamic stall under Darrieus-type Pitching Motion (DPM): High-fidelity CFD simulations are used to conduct a detailed flow field analysis, with DPM segmented into four distinct phases to systematically examine the inception, development, and evolution of dynamic stall. This phased approach provides a comprehensive understanding of dynamic stall characteristics in VAWT blades.

(2) Development of GPR-based ASO framework for VAWT blades: GPR surrogate models are constructed using high-fidelity aerodynamic data are iteratively refined using the Expected Improvement (EI) criterion with sample augmentation. Model accuracy is validated via NRMSE. GA is used to obtain the optimal solution. This framework reduces the optimization cost of ASO.

(3) Dynamic stall optimization of VAWT blades using DPM: Aerodynamic hysteresis loops are characterized through single-blade DPM simulations. The average aerodynamic force is adopted as the optimization objective, effectively mitigating violent force fluctuations and yielding an aerodynamically superior airfoil configuration.

The remainder of this paper is structured as follows: Section 2 introduces the concept of Darrieus-type Pitching Motion (DPM) for VAWTs. Section 3 outlines the SBO framework for ASO, including problem formulation, GPR model development, and optimization workflow. Section 4 details the high-fidelity CFD methodology and validation procedures. Section 5 presents and analyzes optimization results, featuring GPR model validation, comparative airfoil geometry assessment, and flow field diagnostics. Finally, section 6 concludes with principal findings.

2. Darrieus type pitching motion in VAWT

In this study, a straight-blade H-type Darrieus VAWT is considered. The geometry of the three-bladed VAWT and the force analysis at four representative azimuthal positions are shown in Fig 1. The blades are arranged on a circular path of radius R and rotate at a speed of ω. The incoming wind velocity is V_∞, providing the aerodynamic force required to drive the rotor. The angle of attack, defined as the angle between the relative wind velocity and the airfoil chord, varies continuously with blade rotation. The lift force F_L, which constitutes the main contribution to the blade motion, also varies with the blade azimuth angle θ.

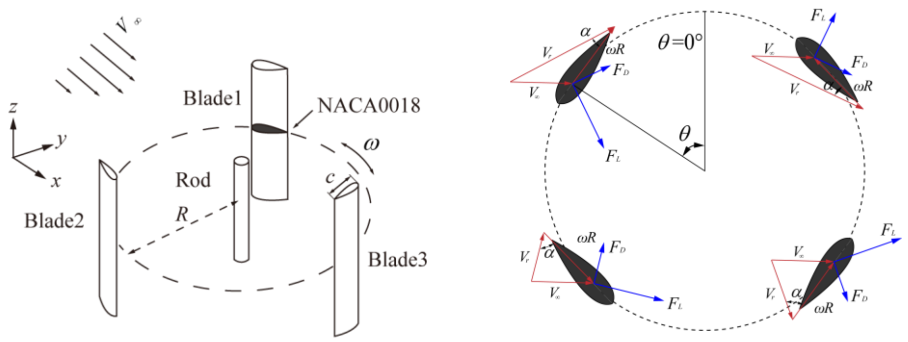

Fig 1. The geometric parameters and force analysis of a H-type Darrieus VAWT

Five dimensionless parameters were used to fully describe the performance of the VAWT. They are [53]: torque coefficient (C_T), power coefficient (C_p), blade tip speed ratio (TSR or λ), Reynolds number (Re) and rotor solidity (σ). The mathematical equations for these parameters are as follows:

$$C_T = T/\left(0.5\rho V_\infty^{\ 2} AR\right) \tag{1}$$

$$C_P = T\omega/\left(0.5\rho V_\infty^{\ 3} A\right) \tag{2}$$

$$\lambda = \omega R/V_\infty \tag{3}$$

$$Re = V_\infty D/\nu \tag{4}$$

$$\sigma = Nc/D \tag{5}$$

where D is the rotor diameter, v is the dynamic viscosity of the air, and N is the number of blades.

From Eqs. (1) to (3), a functional relationship is obtained between C_T, λ and C_p. C_p can also be expressed in the form of Eq. (6):

$$C_P = C_T \cdot \lambda \tag{6}$$

The angle of attack (α) of the blade, defined as the angle between the blade chord line and the relative wind direction, can be determined based on the blade's azimuthal position and the direction of the relative velocity. The relative velocity is calculated as the vector difference between the blade's rotational velocity ($\overline{\omega R}$) and the incoming wind velocity ($\overline{V_\infty}$):

$$\overline{V_r} = \overline{V_\infty} - \overline{\omega R} \tag{7}$$

As the VAWT rotates, the angle of attack experienced by the airfoil varies continuously with the azimuthal position. This motion is often referred to as Darrieus motion [54]. The magnitude of α in Darrieus motion can be expressed as a function of the tip speed ratio (λ) and azimuthal angle (θ) as [55]:

$$\alpha = \tan^{-1}\left(\frac{sin(\theta)}{cos(\theta)+\lambda}\right) \tag{8}$$

The theoretical angle of attack for each azimuthal position at different TSRs can be calculated using to Eq. (8). The airfoil's angular velocity is then obtained by solving the time derivative of Eq. (8) and shown in Eq. (9), where $\theta = \omega t$.

$$\dot{\alpha} = \frac{\omega(\lambda cos(\omega t)+1)}{\lambda^2 + 2\lambda cos(\omega t)+1} \tag{9}$$

Taking λ = 2 as an example, the variation of the angle of attack (AOA) for VAWT blades can be divided into four distinct phases, as shown in Fig 2. When the airfoil rotates clockwise, the angle between the chord line and the incoming flow is considered positive, with the sign of the AOA indicating its direction. Several key observations are noted:

1. Phases 1 and 3: In both phases, the AOA increases from 0° to 30°. However, Phase 3 lasts only half as long as phase I, corresponding to T/6.

2. Phases 2 and 4: The AOA decreases from 30° to 0° in both phases. The descent in Phase 2 occurs more rapidly, also lasting only T/6.

3. Time-dependent variation: For of 0 < t/T < 0.5, the AOA exhibits a slow increase followed by a rapid decrease process. Conversely, for 0.5 < t/T < 1.0, the AOA exhibits a rapid increase followed by a slower decrease process. These variations in the rates of change affect flow attachment and the onset of dynamic stall phenomena.

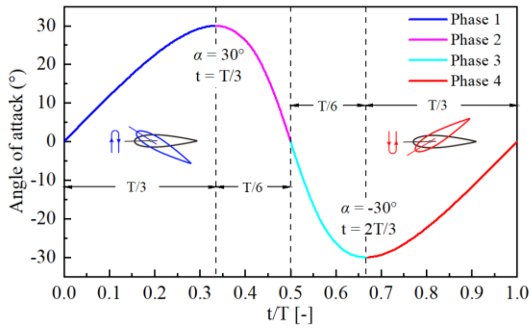

Fig 2. The four phases of variation in angle of attack in one cycle when TSR is 2

3. Aerodynamic shape optimization design method

This section presents a surrogate-based optimization methodology aimed at delaying dynamic stall in an airfoil. The airfoil shape optimization process is specifically described in detail, including

PARSEC parameterization, GPR surrogate modeling, points infill criteria, and surrogate model validation.

3.1 Optimization problem statement

Compared to the sinusoidal curve, this research shows the normalized variation of the angle of attack and angular velocity of the airfoil over one pitching cycle, as shown in Fig 3. In Fig 3a, for 0 < t/T < 0.5, the normalized angle of attack curve lacks the symmetry axis about t/T = 0.25 observed in the sinusoidal curve. Moreover, as the TSR decreases, the maximum angle of attack shifts closer to t/T = 0.5. Fig 3b shows that while the angular velocity of the sinusoidal pitching motion varies smoothly, the angular velocity of the DPM exhibits a sharp slope at t/T = 0.5, indicating a more abrupt change in the angle of attack. This effect becomes increasingly pronounced as the decrease of the TSR decreases.

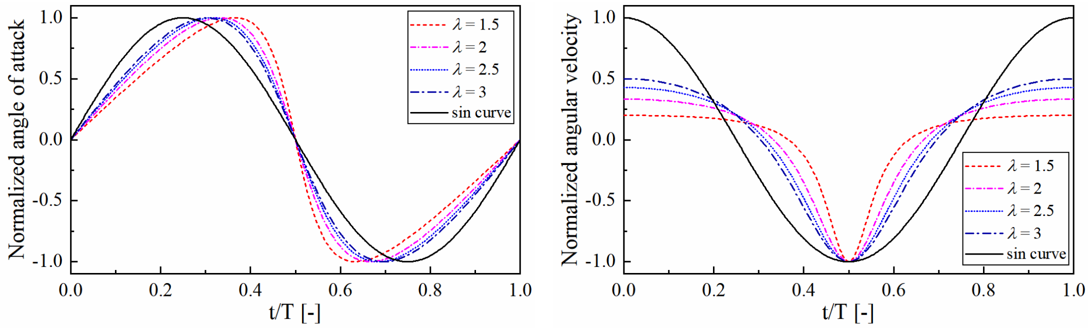

(a) (b)

Fig 3. Normalized variation of VAWT blade within one cycle at different TSRs for (a) angle of attack and (b) angular velocity

Traditionally, the dynamic stall of airfoils has been studied using sinusoidal pitching motion due to the simplicity of the sine function. However, to more effectively address the dynamic stall caused by VAWT rotation, the more complex DPM must be examined, and improvement in dynamic stall characteristics should be addressed through airfoil shape optimization.

With the design objective of delaying the dynamic stall caused by DPM, this study formulates the problem in mathematical terms by defining an objective function and a set of constraints within an airfoil aerodynamic shape optimization method. ASO, which involves modifying the airfoil geometry to maximize the better aerodynamic performance, is therefore applied. A key challenge is to identify the critical airfoil shape parameters and systematically evaluate their influence on the onset and progression of dynamic stall.

The airfoil shape parameters are obtained using parametric methods, whose primary purpose is to represent the geometric shape of an airfoil with reduced number of design variables. Generally, four parametric methods are commonly applied: the Hicks-Hence method, Splines, CST and the PARSEC method. Among these, the PARSEC airfoil parameterization technique defines a set of design variables that directly control the geometric features of the airfoil, including the leading edge radius, maximum thickness and its chordwise position, surface curvature and trailing edge wedge angle. The airfoil geometry described by the 12 PARSEC parameters is shown in Fig 4.

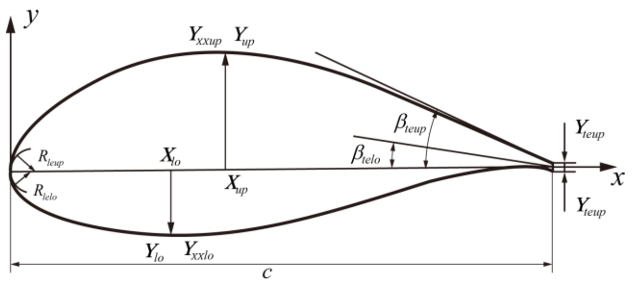

Fig 4 The PARSEC airfoil geometry parameters

Unlike other parameterization techniques such as bump functions [65], b-splines [66] or free-form deformations [67], the PARSEC method offers parameters with clear geometric description. The PARSEC parameters are summarized in Table 1.

Table 1 The description of PARSEC parameters

Parameters	**Description**	**Unit**
R_{leup} , R_{lelo}	Upper (Lower) surface leading edge radius	-
X_{up} , X_{lo}	Upper (Lower) crest position in x coordinates	-
Y_{up} , Y_{lo}	Upper (Lower) crest position in y coordinates	-
Y_{xxup} , Y_{xxlo}	Upper (Lower) surface second-order derivative at X, $\frac{d^2y}{dx^2}\Big\|_{x=X}$	-
Y_{teup} , Y_{telo}	Upper (Lower) surface Trailing edge offset in y coordinates	-
β_{teup} , β_{telo}	Upper (Lower) surface Trailing edge wedge angle	deg

In PARSEC, the upper and lower surface coordinates are expressed as linear combinations of polynomial basis functions, as follows:

$$y_s = \sum_{n=1}^{6} a_s^n x_c^{n-1/2} \qquad s = up, lo \tag{10}$$

where y_s is the y coordinates of upper and lower surface, the subscript s represents the upper (up) and lower (lo) surfaces of the airfoil, a_n^s is the geometric coefficients, which needs to be calculated, and x_c is the dimensionless chordwise position ($0 \le x_c \le 1$).

As an example, for the airfoil upper surface, the PARSEC parameters are obtained by constructing the coefficient matrix associated with Eq. (11).

$$\begin{bmatrix} 1 & 0 & 0 & 0 & 0 & 0 \\ 1 & 1 & 1 & 1 & 1 & 1 \\ x_{up}^{1/2} & x_{up}^{3/2} & x_{up}^{5/2} & x_{up}^{7/2} & x_{up}^{9/2} & x_{up}^{11/2} \\ \frac{1}{2} & \frac{3}{2} & \frac{5}{2} & \frac{7}{2} & \frac{9}{2} & \frac{11}{2} \\ \frac{1}{2}x_{up}^{-1/2} & \frac{3}{2}x_{up}^{1/2} & \frac{5}{2}x_{up}^{3/2} & \frac{7}{2}x_{up}^{5/2} & \frac{9}{2}x_{up}^{7/2} & \frac{11}{2}x_{up}^{9/2} \\ -\frac{1}{4}x_{up}^{-3/2} & \frac{3}{4}x_{up}^{-1/2} & \frac{15}{4}x_{up}^{1/2} & \frac{35}{4}x_{up}^{3/2} & \frac{63}{4}x_{up}^{5/2} & \frac{99}{4}x_{up}^{7/2} \end{bmatrix} \times \begin{bmatrix} a_{up}^1 \\ a_{up}^2 \\ a_{up}^3 \\ a_{up}^4 \\ a_{up}^5 \\ a_{up}^6 \end{bmatrix} = \begin{bmatrix} \sqrt{2R_{leup}} \\ y_{te} \\ y_{up} \\ \beta_{te,up} \\ 0 \\ y_{xxup} \end{bmatrix} \tag{11}$$

The symmetric airfoil NACA0018, commonly used as a VAWT blade profile, is selected as the case study. The PARSEC parameters obtained from Eq. (11) are shown in Table 2. The fitting curve obtained by Eq. (10) is presented in Fig 5, together with the corresponding fitting error. Where Δy denotes the difference in vertical coordinates between the original NACA0018 profile and the fitted curve. As shown in Fig 5b, although the fitting error near the airfoil leading edge is larger due to the high curvature, the overall airfoil geometry is accurately captured and the representation is sufficient for the purpose of this study.

Table 2. PARSEC parameters of NACA0018

Parameters	Values	Parameters	Values
R_{leup}	0.0893	R_{lelo}	0.0893
X_{up}	0.3615	X_{lo}	0.3615
Y_{up}	0.1349	Y_{lo}	-0.06
Y_{xxup}	-0.62	Y_{xxlo}	-0.62
Y_{teup}	0.0028	Y_{telo}	-0.0018
β_{teup}	-6.089	β_{telo}	28

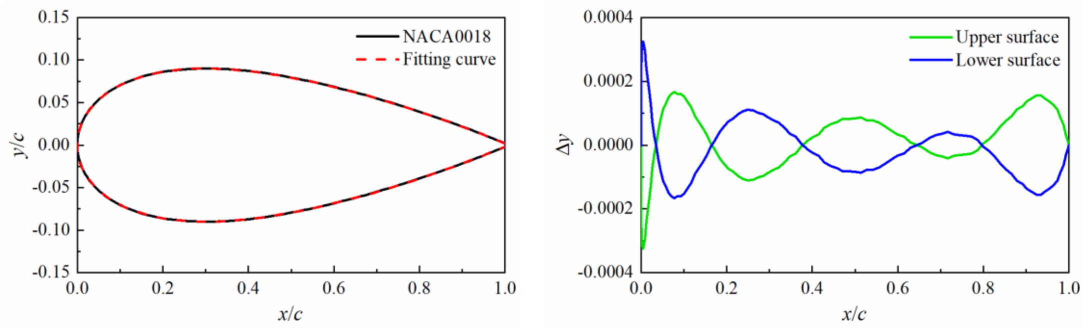

(a) (b)

Fig 5. Results of CST parameterization for S809: (a) geometric shapes between S809 and S809_fitting, (b) airfoil fitting error of upper and lower surfaces

The 12 PARSEC parameters constitute the design variable vector for airfoil optimization and are written as:

$$x = \left[R_{leup}, X_{up}, Y_{up}, Y_{xxup}, Y_{teup}, \beta_{teup}, R_{lelo}, X_{lo}, Y_{lo}, Y_{xxlo}, Y_{telo}, \beta_{telo} \right]^T \tag{12}$$

The bounds of the design variables, as listed in Table 3, are imposed to constrain the parametric variations within aerodynamically feasible limits while still allowing sufficient exploration of the design space. The corresponding geometric design space for the NACA0018 baseline configuration is depicted in Fig 6, which highlights the feasible envelope for shape modifications.

Table 3. Design variable bounds for airfoil upper and lower surfaces

Design variables	Upper bound	Lower bound	Design variables	Upper bound	Lower bound
R_{leup}	0.0893	0.0164	R_{lelo}	0.0893	0.0164
X_{up}	0.3615	0.2505	X_{lo}	0.3615	0.2505
Y_{up}	0.1349	0.06	Y_{lo}	-0.06	-0.1348
Y_{xxup}	-0.62	-0.8	Y_{xxlo}	-0.62	-0.8
Y_{teup}	0.0028	0.0018	Y_{telo}	-0.0018	-0.0028
β_{teup}	-6.089	-28	β_{telo}	28	6.089

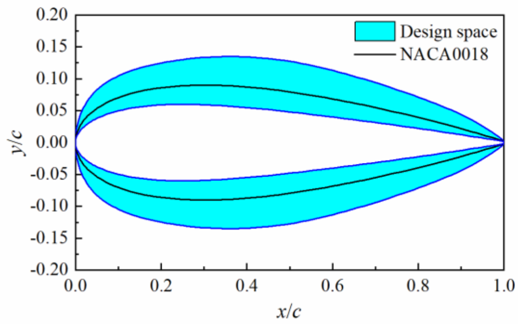

Fig 6. Geometric design space for the NACA0018 airfoil

The primary optimization objective is to determine an airfoil geometry that mitigates dynamic stall risk by attenuating transient aerodynamic load fluctuations. Dynamic stall associated with large variations in drag (C_d) and moment (C_m) coefficients, which can compromise structural integrity and accelerate fatigue damage. Accordingly, this study formulates the objective function to minimize the cycle-averaged aerodynamic coefficients over one DPM oscillation period:

$$F(\boldsymbol{x}) = \min\left[0.6\left(\frac{1}{\boldsymbol{N}}\sum_{\boldsymbol{i}=1}^{\boldsymbol{N}}\left|C_{di}\right|\right) + 0.4\left(\frac{1}{\boldsymbol{N}}\sum_{\boldsymbol{i}=1}^{\boldsymbol{N}}\left|C_{mi}\right|\right)\right] \tag{13}$$

$$\boldsymbol{s.t.}\begin{cases} 0.85T_{\max}^{0} \le T_{\max} \le 1.15T_{\max}^{0} \\ \sum_{\boldsymbol{i}=1}^{\boldsymbol{N}}\left|C_{di}\right| \le \sum_{\boldsymbol{i}=1}^{\boldsymbol{N}}\left|C_{di}^{0}\right| \\ \sum_{\boldsymbol{i}=1}^{\boldsymbol{N}}\left|C_{mi}\right| \le \sum_{\boldsymbol{i}=1}^{\boldsymbol{N}}\left|C_{mi}^{0}\right| \\ \sum_{\boldsymbol{i}=1}^{\boldsymbol{N}}\left|C_{li}\right| \ge \sum_{\boldsymbol{i}=1}^{\boldsymbol{N}}\left|C_{li}^{0}\right| \end{cases} \tag{14}$$

where N is the number of instantaneous AoA per pitching cycle. $T_{\max}$ represents the maximum airfoil thickness. Superscript "0" denotes baseline airfoil parameters. Given the blade AoA variation range of -30°~30°, aerodynamic forces are averaged using absolute AoA values to ensure directionally consistent performance metrics.

3.2. Surrogate modeling using Gaussian process regression

The surrogate-based aerodynamic shape optimization (ASO) procedure is illustrated in Fig 7 and consists of the following steps are:

Step 1 (Parameterization): The PARSEC method is used to represent the blade geometry, with resulting parameters serving as the design variables.

Step 2 (Sampling): An optimized Latin Hypercube Sampling (OLHS) method is employed to generate the initial sample set, denoted as $\boldsymbol{x}$.

Step 3 (CFD Evaluation): For such design samples, computational meshes are generated and CFD simulations are performed to obtain the corresponding aerodynamic force coefficients, denoted as $\boldsymbol{y}$.

Step 4 (Surrogate model construction): A Gaussian Process Regression (GPR) surrogate model is trained using the initial sample set ($\boldsymbol{x}$, $\boldsymbol{y}$).

Step 5 (Adaptive sampling): New sample points are sequentially added in the design space based on the Expected Improvement (EI) criterion. Each new point is evaluated via CFD simulations, and the dataset is iteratively updated to retain and refine the surrogate model.

Step 6 (Optimization and convergence): The optimization objective and constraints are defined, and a GA is applied to each updated surrogate model to identify the best solution. Convergence is monitored using the normalized root mean square error (NRMSE), with a convergence threshold set to 3%.

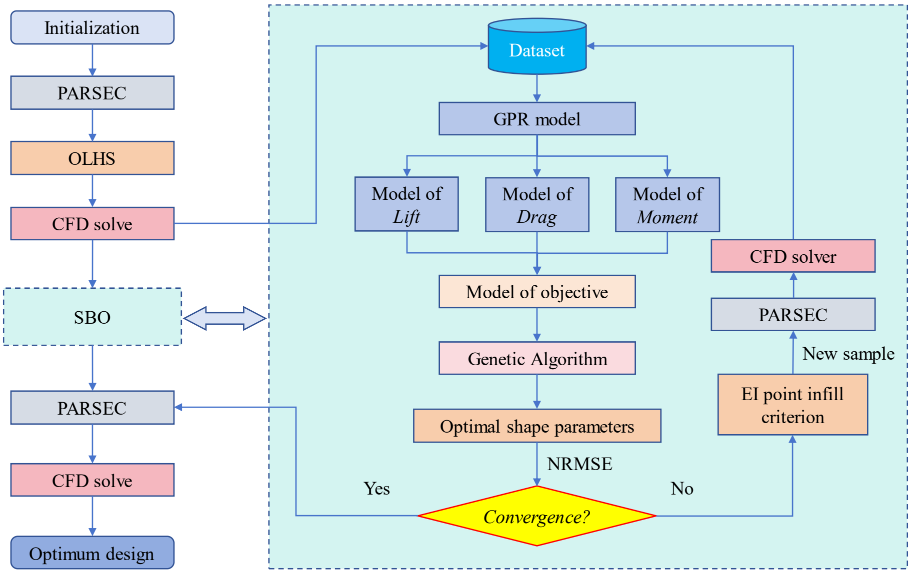

Fig 7. A flowchart of the surrogate-based optimization design

The optimization process is implemented using a MATLAB script that integrates and couples the various modules. The CFD module is automated through macro commands, which handles both parameter setup and data processing. The following subsection presents a detailed description of the individual components involved in constructing the surrogate model.

3.2.1. Sampling method

Latin Hypercube Sampling (LHS) [56], a classical sampling technique, is employed to generate initial sample points for surrogate model construction. To address sample clustering issues that arise in high-dimensional design spaces, we adopt Optimized Latin Hypercube Sampling (OLHS), which maximizes the minimum inter-sample distance. This criterion ensures a more uniform spatial distribution of initial samples throughout the design space [57]. The OLHS sampling can be summarized as:

Let n denote the number of samples and d the dimensionality of the design space. LHS is first used to construct an $n \times d$ sampling matrix, where each column vector is a random permutation of the integers {1, 2, ..., n}. The resulting matrix is then normalized to the interval [0, 1), as follows [58]:

$$L_{ij} = \frac{1}{n}\left(\pi_{ij} - U_{ij}\right) \tag{15}$$

where π_{ij} is a random arrangement of {1, 2, ..., n}, and U_{ij} is a uniform random number in the interval [0, 1).

If there are two sample points z_{ik} and z_{jk} in the space, the Euclidean distance is calculated as follows:

$$d_{ij} = \sqrt{\sum_{k=1}^{d}\left(z_{ik} - z_{jk}\right)^2} \tag{16}$$

Fig 8 illustrates the spatial distributions of sample points in three-dimensional design space, generated using LHS and OLHS. The visualization highlights the pronounced clustering characteristic of conventional LHS, where OLHS achieves a more uniform spatial coverage. This enhanced distribution captures richer geometric information, thereby improving the fidelity of the initial surrogate model fidelity. Furthermore, previous studies suggest that the sample sizes should exceed at least three times the number of design variables to ensure robust surrogate modeling [61, 62]. Accordingly, 200 initial samples were selected for use, substantially surpassing this threshold of 36 (12 design variables × 3) to ensure high-precision model construction.

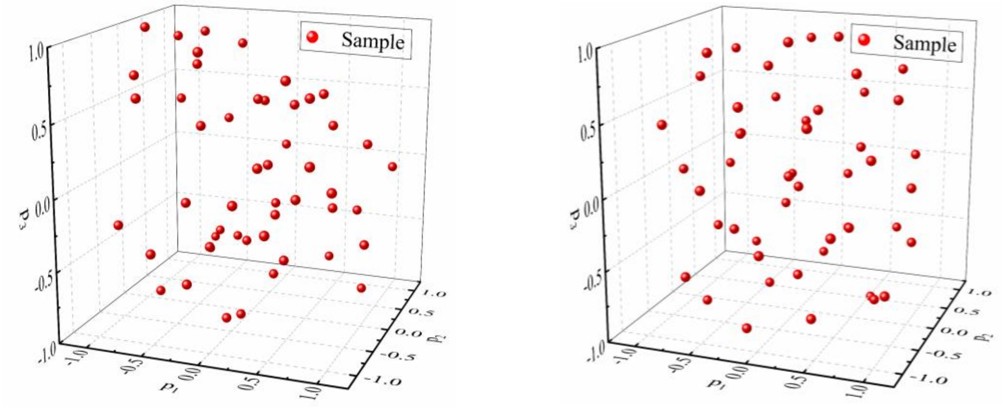

(a) (b)

Fig 8. Samples distribution of LHS and OLHS methods sampling in 3D space

3.2.2. Gaussian process regression model

GPR is a Bayesian, nonparametric method that places a Gaussian process prior on the latent function mapping inputs to outputs. It is particularly well-suited to modelling complex stochastic processes and to problems with small to moderate training set sizes [63]. Given a training dataset $D=\{(\boldsymbol{x}_i,\boldsymbol{y}_i)|i=1,2,\cdots,n\}$, where $\boldsymbol{x}_i$ represents the input matrix composed of training sample points and y_i denotes the corresponding output (response) value, the GPR model can be formulated as [64]:

$$\boldsymbol{y}_i = f(\boldsymbol{x}_i)+\varepsilon_i \tag{17}$$

where $\varepsilon_i \sim N(0,\sigma_n^2)$ is a Gaussian noise with mean value 0 and variance σ_n^2, which captures local variations with a defined covariance structure. The $f(x_i)$ is the mean function representing the global trend, it is assumed to follow a Gaussian Process (GP):

$$f(x_i) \sim GP(\mu(x_i), cov(x_i, x_i'))\tag{18}$$

The Gaussian process is determined by the mean $\mu(\boldsymbol{x}_i)$ and covariance function $\mathrm{cov}(\boldsymbol{x}_i,\boldsymbol{x}_i')$, which is defined as:

$$\mu(\boldsymbol{x}_i)=E(f(\boldsymbol{x}_i))\tag{19}$$

$$\mathrm{cov}(\boldsymbol{x}_i,\boldsymbol{x}_i')=E\left[f(\boldsymbol{x}_i)-\mu(\boldsymbol{x}_i)(f(\boldsymbol{x}_i')-\mu(\boldsymbol{x}_i'))\right]\tag{20}$$

In the absence of observation noise, the prior distribution of the training output $f(x_i)$ is defined as a multivariate Gaussian random vector as $f(x_i) \sim GP(0，cov())$. For a test input $\boldsymbol{x}_i^*$, the joint prior distribution of the training output y_i is given by the multivariate Gaussian distribution:

$$\begin{pmatrix}\boldsymbol{y}_i\\ \boldsymbol{y}_i^*\end{pmatrix} \sim GP\left(0,\begin{pmatrix}\mathrm{cov}(\boldsymbol{x}_i,\boldsymbol{x}_i) & \mathrm{cov}(\boldsymbol{x}_i,\boldsymbol{x}_i^*)\\ \mathrm{cov}(\boldsymbol{x}_i^*,\boldsymbol{x}_i) & \mathrm{cov}(\boldsymbol{x}_i^*,\boldsymbol{x}_i^*)\end{pmatrix}\right)\tag{21}$$

where y_i^* is the predicted output corresponding to a test input, $\mathrm{cov}(\boldsymbol{x}_i, \boldsymbol{x}_i)$ is the covariance matrix of the training data, $\mathrm{cov}(\boldsymbol{x}_i, \boldsymbol{x}_i^*)$ and $\mathrm{cov}(\boldsymbol{x}_i^*, \boldsymbol{x}_i)$ represent the cross-covariance between the training and test inputs, and $\mathrm{cov}(\boldsymbol{x}_i^*, \boldsymbol{x}_i^*)$ is the covariance between the test samples. In the Gaussian process framework, the predictive distribution is derived from the joint prior by conditioning on the observed training dataset *D* are known, as follows:

$$y_i^* | x_i^*,\ D \sim GP(\mu_{y_i^*},\ \Sigma_{y_i^*}) \tag{22}$$

where：

$$\mu_{y_i^*} = \mathrm{cov}(\boldsymbol{x}_i^*, \boldsymbol{x}_i)\left(\mathrm{cov}(\boldsymbol{x}_i^*, \boldsymbol{x}_i^*) + \sigma_n^2 \boldsymbol{I}_E\right)^{-1} y_i \tag{23}$$

$$\begin{aligned}\Sigma_{y_i^*} = {} & \mathrm{cov}(\boldsymbol{x}_i^*, \boldsymbol{x}_i) - \mathrm{cov}(\boldsymbol{x}_i^*, \boldsymbol{x}_i)\Big(\mathrm{cov}(\boldsymbol{x}_i^*, \boldsymbol{x}_i^*) \\ & + \sigma_n^2 \boldsymbol{I}_E\Big)^{-1} \mathrm{cov}(\boldsymbol{x}_i, \boldsymbol{x}_i^*)\end{aligned} \tag{24}$$

To calculate the posterior mean $\mu_{y_i^*}$ and variance $\Sigma_{y_i^*}$ in GPR, it is essential to evaluate the four covariance terms, which are defined by the kernel function. Various forms of kernel functions can be employed in regression models. Commonly used kernel functions include RBF kernel, matern kernel, Periodic kernel, et al. The matern kernel provides greater flexibility in modeling and its suitable for nonlinear data, so it was adopted in our research [65].

The edge probability $p(y_i^* | \boldsymbol{x}_i^*)$ is an important parameter in GPR modeling, as follows:

$$p(y_i^* | \boldsymbol{x}_i^*) = N\left(0, \mathrm{cov}(\boldsymbol{x}_i, \boldsymbol{x}_i) + \sigma_n^2 \boldsymbol{I}_E\right) \tag{25}$$

A GPR model is fitted to the given sample dataset. The hyperparameters of the kernel function are estimated by maximizing the log marginal likelihood, which is defined as:

$$L(\theta) = -\log p(y_i | \mathbf{x}_i, \theta) = \frac{1}{2} y_i^T C^{-1} y_i + \frac{1}{2}\log|C| + \frac{n}{2}\log 2\pi \tag{26}$$

where, $C = \mathrm{cov}(\boldsymbol{x}_i, \boldsymbol{x}_i) + \sigma_n^2 \boldsymbol{I}_E$, the C is the covariance matrix computed using the kernel function with hyperparameters θ, n is the number of training samples. Maximizing this function with respect to θ allows the model to best fit the observed data under the assumed Gaussian prior.

3.2.3. Expectation improvement Infill criteria

The quality of the optimization results depends strongly on the accuracy of the surrogate model. A GPR model constructed from a limited set of initial samples may exhibit large prediction errors in certain regions of the design space. Expanding the number of initial samples through global modeling is often computationally expensive. A more efficient alternative is to selectively introduce new samples in regions where the prediction error is expected to be high, thereby improving local accuracy.

To address this challenge, an adaptive sampling strategy is employed, which progressively refines the surrogate model by incorporating additional samples based on a sampling criterion. In this study, the Expected Improvement (EI) criterion, originally proposed by Jones [66], is adopted to guide the local exploration of the design space. The key advantage of the EI method lies in its ability to identify locations that are most likely to contribute to improving the surrogate model.

For the GPR model, the EI at a candidate point x is calculated using the predicted mean $\bar{y}(x)$ and standard deviation s^2 as follows [67]:

$$E(\boldsymbol{I}(\boldsymbol{x}))=\int_0^{+\infty}\boldsymbol{I}(\boldsymbol{x})\cdot\phi(\boldsymbol{I}(\boldsymbol{x}))d\boldsymbol{I}$$
$$=\begin{cases}(y_{\min}-\overline{y})\Phi\left(\dfrac{y_{\min}-\overline{y}}{s}\right)+s\phi\left(\dfrac{y_{\min}-\overline{y}}{s}\right) & s>0\\ 0 & s=0\end{cases} \tag{27}$$

where Φ and ϕ denote the cumulative distribution function and the probability density function of the standard normal distribution, respectively. Let $y_{\min}$ represent the current best (minimum) objective function value observed. The improvement $\boldsymbol{I}(\boldsymbol{x})$ is expressed as:

$$\boldsymbol{I}(\boldsymbol{x})=y_{\min}-\overline{y}(\boldsymbol{x}) \tag{28}$$

The GPR prediction result $\hat{y}(\boldsymbol{x})$ obeys a Gaussian distribution with mean $\overline{y}(\boldsymbol{x})$ and variance s^2, in the form of $\hat{y}(\boldsymbol{x})\in N[\overline{y}(\boldsymbol{x}),s^2]$. Its probability density function is:

$$\phi(\hat{y}(\boldsymbol{x}))=\frac{1}{\sqrt{2\pi}s(\boldsymbol{x})}\exp\left(-\frac{1}{2}\left(\frac{\hat{y}(\boldsymbol{x})-\overline{y}(\boldsymbol{x})}{s(\boldsymbol{x})}\right)\right) \tag{29}$$

The next infill point is selected by maximizing the $E(\boldsymbol{I}(\boldsymbol{x}))$ function using a global optimization algorithm [68]. In summary, new sample points are iteratively selected based on the EI criterion to enhance the accuracy of the surrogate model. Each selected point is then evaluated using high-fidelity CFD simulations and added into the existing dataset to update and reconstruct the surrogate model. This iterative process is repeated continues until the surrogate model satisfies the predefined accuracy threshold.

3.3.4. Surrogate model validation

The accuracy of the surrogate model is further evaluated using the Normalized Root Mean Square Error (NRMSE), which has the advantage of being insensitive to difference in data magnitudes and units. The NRMSE is defined as:

$$\mathrm{NRMSE}=\frac{\sqrt{\dfrac{1}{n_t}\sum_{i=1}^{n_t}\left(y_t^i-\hat{y}_t^i\right)^2}}{\left(y_{\max}-y_{\min}\right)_{initial}} \tag{30}$$

where, y_t^i denotes the CFD model evaluation value and $\hat{y}_t^i$ represents the corresponding value predicted by surrogate model. The variable n_t is the number of test samples and the $\left(y_{\max}-y_{\min}\right)_{initial}$ represents the range of the initial sample dataset. In this study, the surrogate model is considered sufficiently accurate when the NRMSE is less than or equal to 3%.

4. Numerical methodology for airfoil simulations

4.1 Reference case

For the Darrieus-type pitching motion, Wickens [69] conducted an experimental investigation of the NACA 0018 airfoil in a 2 × 3 m wind tunnel at the Aerodynamics Laboratory of the National Research Council of Canada. A schematic representation of the wind tunnel setup and the Darrieus pitching motion about the aerodynamic center of the airfoil is shown in Fig 9. A control system was employed to precisely implement pitching motions and regulate the pitch motions.

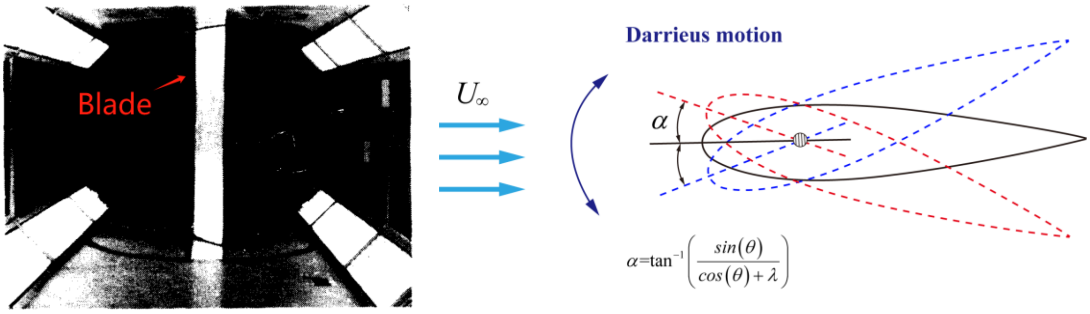

(a) 2m×3m wind tunnel (b) Darrieus type pitching motion

Fig 9. General arrangement of NACA0018 airfoil in the wind tunnel

During the wind tunnel tests, the blade was subjected to an incoming flow velocity of 45.72 m/s, corresponding to a Reynolds number of 1.91 × 10^6. The airfoil had a chord length of 0.61 m. The velocity of 45.72 m/s represents the resultant flow acting on a single blade, taking into account the effects of blade rotation. In essence, the DPM replicates the kinematic behavior of a VAWT blade during rotation. Throughout the experiment, detailed unsteady surface pressure measurements were recorded, from which the normal and tangential force coefficients were subsequently calculated.

4.2 Computational domain topology

The dimensions and boundary conditions of the three-dimensional computational domain are illustrated in Fig 10. The domain is defined as 30c × 60c to ensure the full development of the wake flow. Considering the accuracy limitations of two-dimensional unsteady simulations, this study adopts a quasi-three-dimensional blade model by extruding the NACA0018 airfoil 0.5 chord lengths in the spanwise direction. This configuration offers two key advantages:

(1) It captures spanwise flow effects, significantly improving the accuracy of aerodynamic force predictions.

(2) The limited spanwise extension (0.5c) keeps the mesh size within a computationally feasible range compared to full length blade simulations.

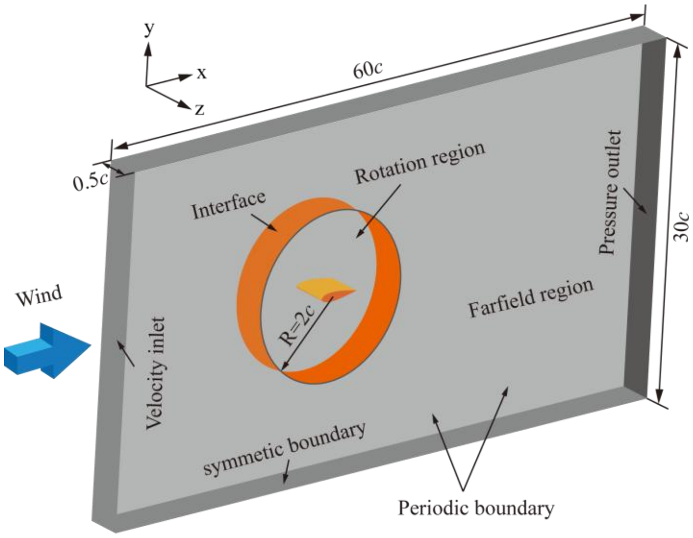

Fig 10. Computational domain topology and boundary conditions

The computational domain is divided into a stationary region and a rotating region, with the rotating zone having a radius of 2*c*. The pitching motion of the rotating region relative to the stationary domain is implemented using a User-Defined Function (UDF) within the solver, in combination with a sliding mesh technique. The boundary conditions are defined as follows: a velocity inlet and pressure outlet are applied at the inflow and outflow boundaries, respectively, while the lateral boundaries are treated as symmetric and periodic conditions.

4.3 Computational grid

A hybrid hexahedral-polyhedral meshing strategy was employed to improve mesh quality and accelerate convergence. Hexahedral cells were used to generate structured boundary layer meshes, while polyhedral cells provided greater flexibility in accommodating complex domain topology and reduced the overall cell count. Fig 11 illustrates the computational mesh and local refinement around the blade surface. The mesh was refined in the vicinity of the blade surface to accurately capture the boundary layer flows associated with dynamic stall phenomena. Additional details regarding grid size and resolution are discussed in the validation section.

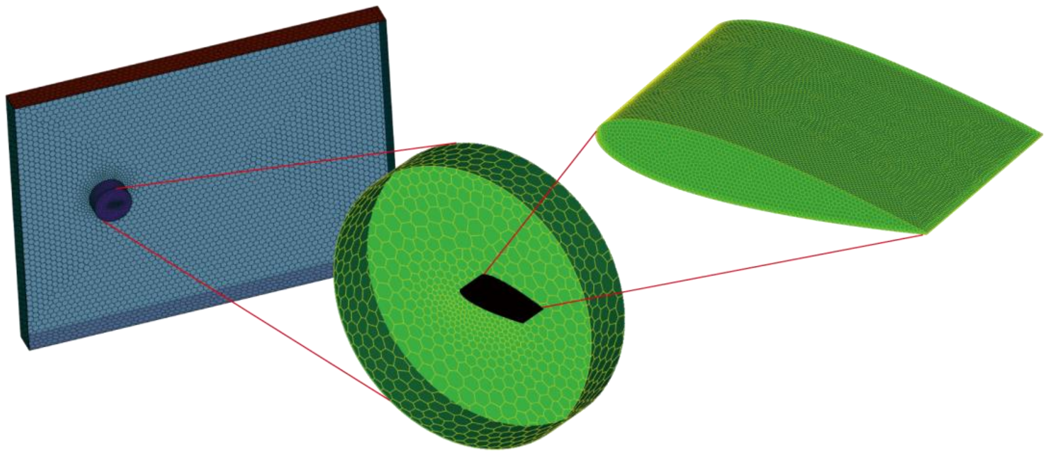

Fig 11. Computational domain grid distribution and detailed view around the NACA0018 airfoil.

4.4 Grid and time independence studies

Mesh quality and time step size are two critical factors that significantly influence the accuracy of CFD simulations. Therefore, it is essential to perform a mesh and time step independence study to determine appropriate resolution, ensuring reliable aerodynamic predictions of dynamic stall under Darrieus-type pitching motion (DPM).

4.4.1 Grid independence study

Grid independence is first investigated by considering four different resolutions, as summarized in Table 4. The parameters examined include the height of the first layer in the boundary layer (H_{BL}), the size of the airfoil's leading edge (S_{LE}), the size of the trailing edge (S_{TE}), the growth rate of the surface grid (R_S), the growth rate of the volume grid (R_V), and the relative size of the interface elements ($\Delta I/c$) are investigated. The mesh is gradually refined with decreasing sizes.

Table 4 Grid independence study

Grid	Number of elements	Boundary Layer element size			Surface grid growth rate	Volume grid growth rate	Interface element size
	N_E	H_{BL} (mm)	S_{LE} (mm)	S_{TE} (mm)	R_S	R_V	$\Delta I/c$
G1	145×10^5	0.04	0.28	0.08	1.10	1.15	0.0553
G2	191×10^5	0.02	0.14	0.04	1.05	1.10	0.0427
G3	227×10^5	0.01	0.07	0.02	1.02	1.05	0.0310
G4	255×10^5	0.01	0.03	0.01	1.02	1.02	0.0283

The lift coefficient (C_l) and drag coefficient (C_d) are key aerodynamic parameters commonly used to evaluate blade performance. Their mathematical definitions are given in Eq (31).

$$C_{l,d} = \frac{F_l, F_d}{0.5\rho U_\infty^2 c} \tag{31}$$

The Unsteady Reynolds Averaged Navier-Stockes (URANS) equations were solved using STAR CCM+ software. The turbulence model was adopted with SST k-ω, and the SIMPLEC algorithm was employed for pressure–velocity coupling.

Fig 12 presents the aerodynamic results over one DPM cycle. Two aerodynamic oscillations are observed within a single cycle, indicating the occurrence of dynamic stall, with the second oscillation lasting longer than the first. The influence of mesh resolution is most noticeable during the unsteady oscillation phases, where more refined meshes are required to accurately capture the complex boundary layer flow. Moreover, the C_d is more sensitive to mesh resolution. Significant deviations are observed between the coarse meshes G1 and G2 during the stall phase, whereas the aerodynamic results obtained from G3 and G4 are very similar, indicating mesh convergence. The discrepancies among different mesh levels are further quantified using the coefficient of determination (R^2).

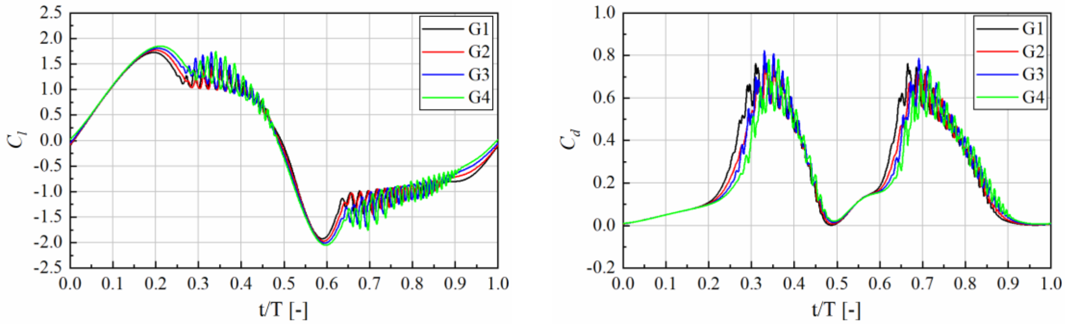

(a) (b)

Fig 12. Results of grid independence verification on the variation of (a) C_l and (b) C_d at different grid numbers

The R^2 was used to characterize the similarity between the two mesh resolutions, with larger values indicating greater similarity. It is calculated based on the drag coefficient as shown in Eq. (32) where C_d^{ref} and C_d^{ave} represent the reference drag coefficient and the average drag coefficient, respectively. The reference drag coefficient is obtained from the results of the previous mesh. The calculated R^2 value are shown in Table 5. As the mesh is refined, the difference in aerodynamic forces decreases. Notably, the R^2 between G3 and G4 is 98.31%, indicating that further refinement beyond G3 has minimal effect on the aerodynamic results. Therefore, the mesh resolution of G3 is selected for subsequent aerodynamic calculations.

$$R^2 = 1 - \frac{\sum_{t=0}^{T}\left(C_d(t) - C_d^{ref}(t)\right)^2}{\sum_{t=0}^{T}\left(C_d(t) - C_d^{ave}\right)^2} \tag{32}$$

Table 5. Coefficient of determination with respect to prior grid

	G2	G3	G4
R^2	0.9052	0.9526	0.9831

4.4.2 Time independence study

In this work, one pitch cycle of the blade actually represents one rotation of the VAWT. Therefore, for the Darrieus dynamic stall of the VAWT, the time step is related to the rotation angle of the VAWT. The times corresponding to VAWT rotations with 0.5°, 0.25° and 0.125° are selected as time steps to analyze the time sensitivity to accurately predict the stall. The detailed parameters of the time steps are shown in Table 6. The simulations are achieved by a 72-core high-performance computing cluster and wall-clock times are recorded. The computation time required increases multiply as the time step decreases.

Table 6. The detailed parameters of time step (λ = 2)

Parameters	Time step	Δt / (10^{-4})	Azimuthal increment (divide into 360°)/ $\Delta\theta$	Wall-clock time/ (hrs)
T1	$2\pi/360\omega$	25.25	0.5°	5.51
T2	$2\pi/720\omega$	12.62	0.25°	11.25
T3	$2\pi/1440\omega$	6.31	0.125°	22.05

The time sensitivity of the Darrieus dynamic stall is investigated at λ = 2 and λ = 3. Fig 13 shows the variation of the lift coefficient in one pitch cycle. At λ = 2, the flow is highly unsteady, necessitating smaller time steps to accurately resolve the simulation. When the time step is reduced from T1 to T2, earlier flow separation is observed, indicating a significant deviation from T1. In contrast, the differences between T2 and T3 in the dynamic stall stage are small, with the predicted flow separation points nearly identical. At the higher TSR as shown in Fig 13b, the aerodynamic forces are more stable and dynamic stall is absent, indicating reduced sensitivity to the time step. Based on these observations, the time step corresponding to T2 is chosen for aerodynamic data acquisition to achieve a balance computational accuracy and time.

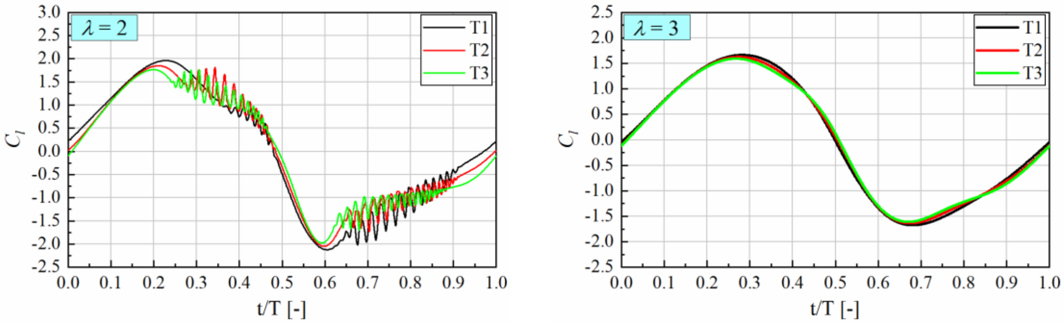

(a) (b)

Fig 13. Results of time sensitivity verification on the variation of (a) λ=2 and (b) λ=3 at different time steps

4.5 Validation with experiment data

The numerical computational method described in Section 4.4 is applied to verify its accuracy in predicting the airfoil aerodynamic forces by comparing the experimental measurements. Fig 14 shows the aerodynamic results at different TSRs and compares with 2D simulation data by Hand et al. The normal (F_n) and tangential (F_t) forces correspond to the structural forces and power generation during VAWT blade operation, respectively. Accurate prediction of these forces is essential for the aerodynamic design and performance analysis of offshore VAWTs. In this section, the blade forces are presented in dimensionless form as normal (C_n) and tangential (C_t) force coefficients.

$$C_{n,t} = \frac{F_n, F_t}{0.5\rho U_\infty^2 c} \tag{33}$$

At $\lambda = 2$, the aerodynamic forces are highly unsteady, with pronounced oscillations, especially at large angles of attack. In Fig 14a, compared to the 2D calculations of Hand et al. [51], the 3D simulations presented in this work predict the stall angle more accurately at 0°-30° and 0°-(-30°). Moreover, the 3D simulation better predicts the dynamic stall of the aerodynamic forces in the range of 30°-0° versus (-30°)-0°, showing closer agreement with experimental values. In Fig 14b it is evident that predicting the C_t is more difficult than C_n, with a significant discrepancies observed in the range of 20°-30° and (-20°)- (-30°). This difficulty has also been reported in the studies by Strickland et al. [70] and Hand et al. [51], and it is attributed to the fact that C_t is an order of magnitude smaller than C_n, making accurate prediction more challenging. Nevertheless, the 3D simulation provides improved accuracy in capturing the dynamic stall, reflecting more detailed flow variations. At $\lambda = 3$, as shown in Fig 14c and Fig 14d, aerodynamic oscillations are absent during pitching, and both C_n and C_t exhibit better agreement with the experimental values, except at large angles of attack where underprediction occurs. Overall, compared to the 2D simulation, the 3D model more accurately reproduces the dynamic stall phenomena.

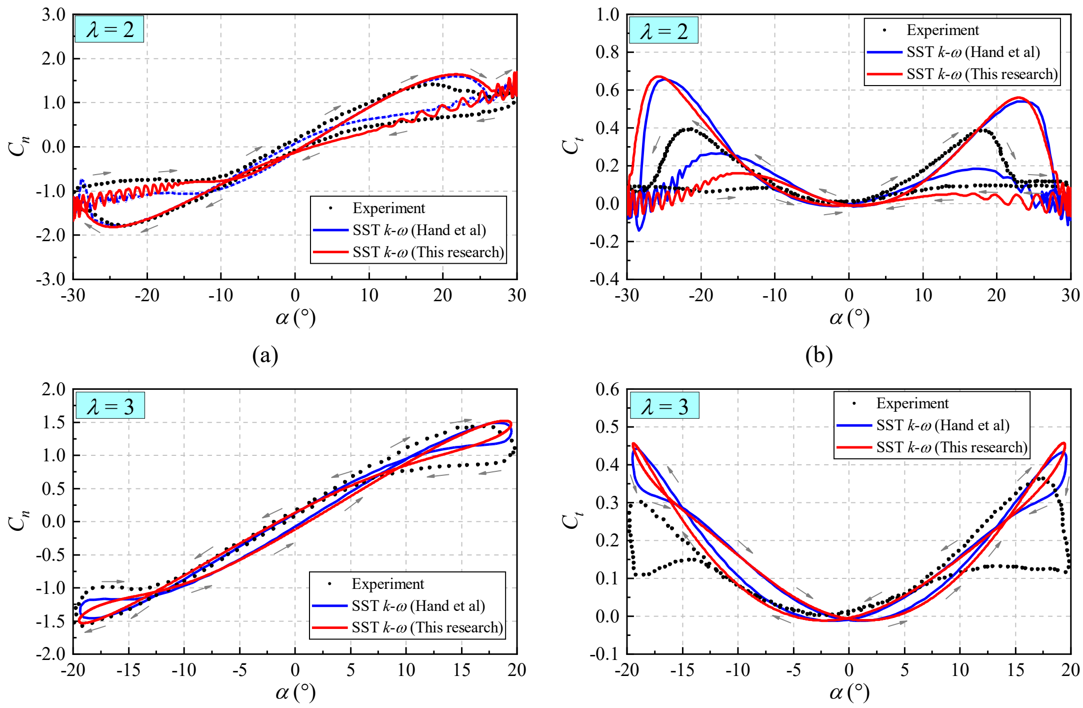

Fig 14. Results of normal and tangential force coefficients at different TSRs with experimental data (2D in literature [51] and 3D in this research).

The pressure coefficients at different angles of attack provides a detailed visualization of the blade surface flow. Fig 15 compares the pressure coefficients obtained from simulations with those measured in wind tunnel experiments. At α=20°↑, the simulated pressure coefficients closely match the experimental values because the blade remains below the stall phase. As the angle of attack increases α=30°↑, differences between the 2D and 3D simulation become apparent. The 2D simulation has underestimates of the pressure at the leading edge. Compared to the 2D, whereas the 3D simulation provides a better fit to the pressure distribution on the upper surface. During the downstroke phase, at α=20°↓, the 2D simulation overestimates the leading edge pressure, indicating instability in its aerodynamic prediction. At α=-20°↓, the 2D simulation struggles to accurately predict the pressure coefficient along the chord in the region 0.1 < x/c < 0.45. In contrast, the 3D simulation improves the accuracy of pressure coefficients prediction by capturing the flow details along the spanwise direction of the blade. The CFD model developed in this paper demonstrates good accuracy. Since the subsequent simulations are performed without add-on devices on the blade surface, this validation supports the reliability of aerodynamic predictions in further investigations.

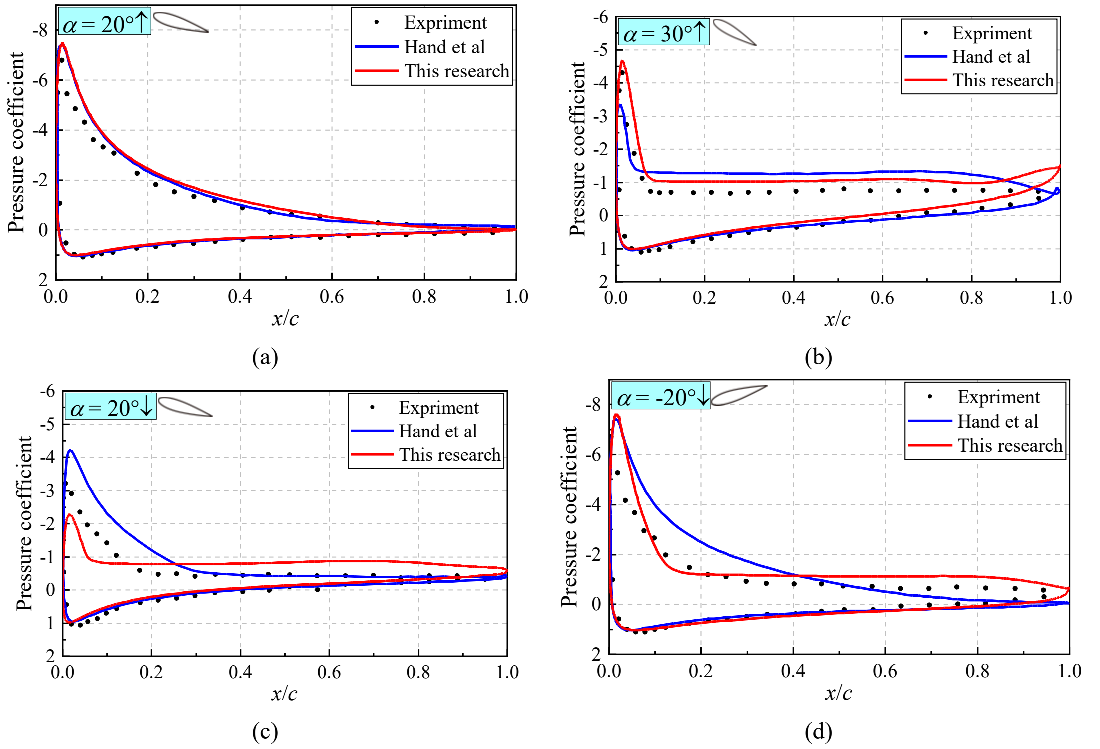

Fig 15. Comparison of pressure coefficients at different angles for experiments and numerical simulations (2D in literature [51] and 3D in this research).

5. Results and discussions

In this section, a GPR-based surrogate model was constructed, and the EI criterion was applied to sequentially infill sample points, resulting in a surrogate model that satisfied the prescribed accuracy requirements. A comparative analysis was then performed between the baseline and optimized airfoils in terms of aerodynamic characteristics and velocity contours. Finally, the Q-criterion method was employed to investigate the near-wall vortex structures in the flow field.

5.1 Surrogate modeling

A GPR model was initially constructed using 200 high-fidelity CFD samples to establish a relationship between blade geometric parameters and aerodynamic performance indicators. The EI criterion was then applied to identify candidate the points with the greatest potential to improve model accuracy. A fixed budget of 60 additional sample points was sequentially introduced, thereby iteratively refining the GPR model.

Fig 16 illustrates the EI-based infill strategy and the corresponding convergence process. A genetic algorithm was employed to search for the global optimum on the surrogate model, with the parameters set as follows: an initial population size of 100, 400 generations, and a mutation rate of 0.02. In Fig 16a, blade optimization was performed on the updated surrogate model after each new sample was added. The optimization results during the GPR+EI process are shown. Since the objective was to minimize average drag and moment coefficients, the optimization results progressively decreased as more samples were added. Although some outliers were observed, the overall trend follows the expected optimization direction. The normalized root mean square error (NRMSE) was used to evaluate surrogate model accuracy. As shown in Fig 16b, after the addition of 60 new samples, the NRMSE of the optimization objective dropped below 3%, demonstrating that both the model accuracy and optimization objectives satisfied the required thresholds. At this point, the optimization process was terminated.

The training time of the surrogate model was nearly negligible, the main computational cost of the entire optimization process arising from the CFD evaluations of both the initial and newly added samples. The optimization was performed on two high-performance computing machines, with each CFD evaluation running on 96 cores. The total computational cost was approximately 2925 CPU hours.

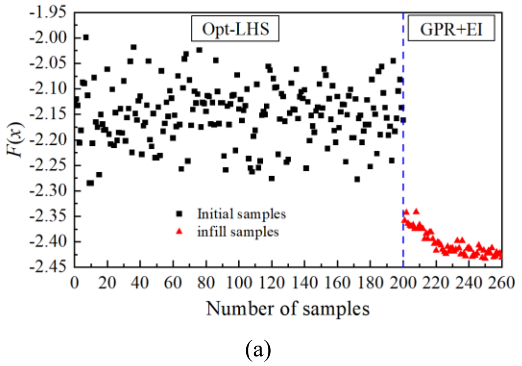

Fig 16. Results of surrogate model construction: (a) is the optimization process of OLHS sampling and GPR+EI, and (b) is the variation in NRMSE with increasing infill samples.

5.2. Aerodynamic force analysis

The baseline airfoil NACA0018 was optimized using the SBO method, resulting in the optimized airfoil OPT180. A comparison of the geometries of NACA0018 and OPT180 is shown in Fig 17, while Table 7 summarizes the variations in design variables (airfoil geometric parameters). Relative to NACA0018, OPT180 exhibits a reduced leading-edge radius, increased maximum thickness, and a rearward shift in the location of maximum thickness. The curvature at the point of maximum thickness undergoes the most significant modification, reflecting an increased camber on both the upper and lower surfaces. In contrast, changes in the trailing-edge deflection angle and trailing-edge thickness are relatively minor. For dynamic stall induced by DPM, the maximum thickness and surface curvature are identified as the two most influential geometric parameters governing aerodynamic performance.

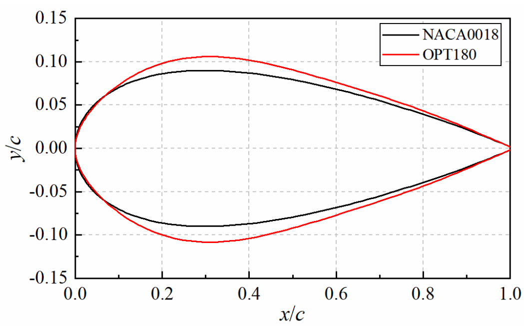

Fig 17. Comparison of airfoil shapes for NACA0018 and OPT180

Table 7. Design variables of NACA0018 and OPT180

Design variables	NACA0018	OPT180	Design variables	NACA0018	OPT180
R_{leup}	0.0328	0.0240	R_{lelo}	0.0328	0.0236
X_{up}	0.3010	0.3082	X_{lo}	0.3010	0.3086
Y_{up}	0.0899	0.1056	Y_{lo}	-0.0899	-0.1079
Y_{xxup}	-0.6610	-1.0894	Y_{xxlo}	0.6610	1.1477
Y_{teup}	0.0019	0.0023	Y_{telo}	-0.0019	-0.0022
β_{teup}	-12.1781	-13.7176	β_{telo}	12.1781	13.8427

Fig 18 compares the aerodynamic coefficients between NACA0018 and OPT180 over a complete DPM cycle. The aerodynamic force oscillations are more intense during the phase 4 (α from −30° to 0°) than in phase 2 (α from 30° to 0°). As shown in Fig 18a, during the upstroke, the C_l of OPT180 exhibits a slight reduction relative to NACA0018. Although OPT180 does not mitigate the frequency of aerodynamic oscillations during stall, it enhances the amplitude of aerodynamic forces within the oscillation range. In Fig 18b, the C_d of OPT180 is significantly lower than that of NACA0018, particularly near the ±30°, where a reduction of up to 40% is achieved. This improvement is attributed to the higher weighting assigned to C_d in the optimization objective, leading to more substantial reductions in drag. In addition, OPT180 decreases the amplitude of the C_m in the stalled region, which contributes to improved aerodynamic stability of the blade.

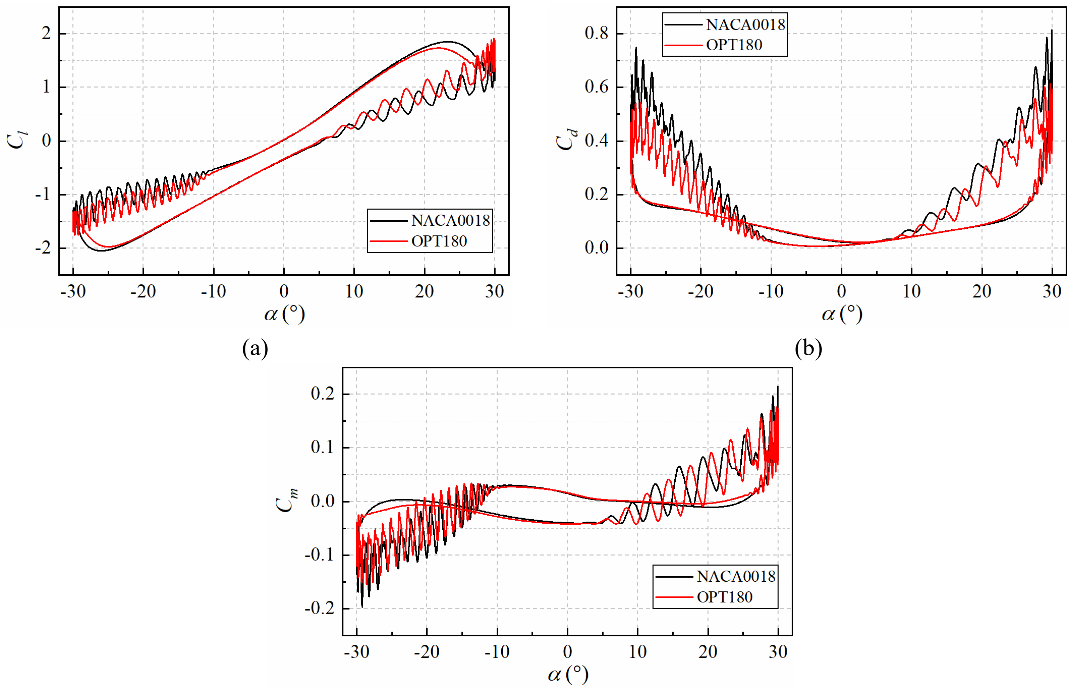

Fig 18. Results of aerodynamic for NACA0018 and OPT180: (a) C_l, (b) C_d, (c) C_m

C_n and C_t are critical parameters governing the rotational performance of a VAWT. C_n plays a key role in ensuring the rotor stability, while C_t contributes directly to the torque generation that drives blade rotation. Fig 19 compares the C_n and C_t of NACA0018 and OPT180 over one DPM cycle. The C_n curve closely exhibits similar trend to that of the C_l. While OPT180 does not increase the amplitude of aerodynamic forces, it effectively reduces aerodynamic losses within the oscillation region. Although NACA0018 exhibits a higher peak value of C_t, it experiences negative values (C_t

<0) during stall, indicating torque reversal. In contrast, OPT180 significantly improves aerodynamic performance during stall, effectively suppressing the generation of negative torque. Furthermore, OPT180 reduces the peak torque coefficient, resulting in a more stable torque output from the blade.

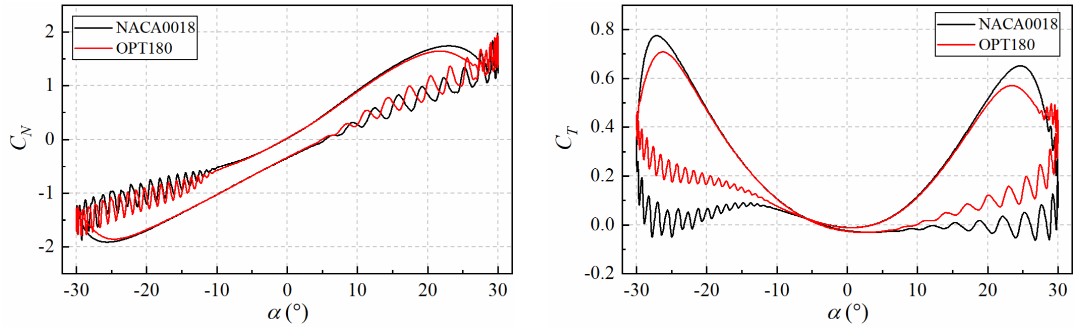

(a) (b)

Fig 19. Results of aerodynamic for NACA0018 and OPT180: (a) C_n, (b) C_t

The average aerodynamic force coefficients of NACA0018 and OPT180 over a full DPM cycle were calculated for all angles of attack, as summarized in Table 8. Since the optimization objective focused on minimizing the average drag coefficient ($|\bar{C}_d|$) and moment coefficient ($|\bar{C}_m|$), OPT180 achieved significant reductions of 18.28% and 12.23%, respectively, compared to NACA0018. Additionally, by applying a constraint on the average lift coefficient ($|\bar{C}_l|$), the $|\bar{C}_l|$ of OPT180 was increased by 3.80%. Although an increase in the average normal force coefficient ($|\bar{C}_n|$) can lead to higher loads on the rotor shaft, OPT180 exhibits only a slight increase of 1.72%. In contrast, the average tangential force coefficient ($|\bar{C}_t|$) of OPT180 improves by 23.87%, indicating a substantial enhancement in torque output. Collectively, these results demonstrate that the aerodynamic shape optimization framework developed in this study successfully produces an airfoil with significantly improved aerodynamic performance.

Table 8. Comparison of average aerodynamic parameters in one dynamic stall cycle

Parameters	$\lvert\bar{C}_l\rvert$	$\lvert\bar{C}_d\rvert$	$\lvert\bar{C}_m\rvert$	$\lvert\bar{C}_n\rvert$	$\lvert\bar{C}_t\rvert$
NACA0018	1.0888	0.2303	0.0458	1.0983	0.2098
OPT180	1.1302	0.1882	0.0402	1.1172	0.2599
Rate of change/%	3.80	-18.28	-12.23	1.72	23.87

5.3. Dynamic stall in one DPM

The Darrieus-type pitching motion (DPM) can be divided into four distinct phases, within which the dynamic stall characteristics of the NACA0018 and OPT180 airfoils are compared individually. Fig 20 shows the pressure coefficient (C_P) distributions of the two airfoils (NACA0018 and OPT180) during Phase 1. The symbols "↑" and "↓" represent the upstroke and downstroke processes, respectively.

Phase 1 corresponds to the increasing angle of attack (α) from 0° to 30°. For α < 26.56°, OPT180 exhibits a slightly reduced leading-edge pressure difference compared with NACA0018 in the region x/c < 0.2. This behavior arise from the smaller leading-edge radius of OPT180, which decreases suction-side flow velocity at lower angles of attack. As α exceeds 26.56°, the leading-edge pressure difference of NACA0018 gradually decreases, while the adverse pressure near the trailing edge increases, indicating the presence of strong separation vortices. In contrast, OPT180 maintains a stable and favorable leading-edge pressure difference despite the increasing angle of attack. This aerodynamic shape modification effectively alters the pressure distribution, leading to improved aerodynamic performance in OPT180. Notably, at α=30°, the peak suction pressure at the leading edge of OPT180 is twice that of NACA0018.

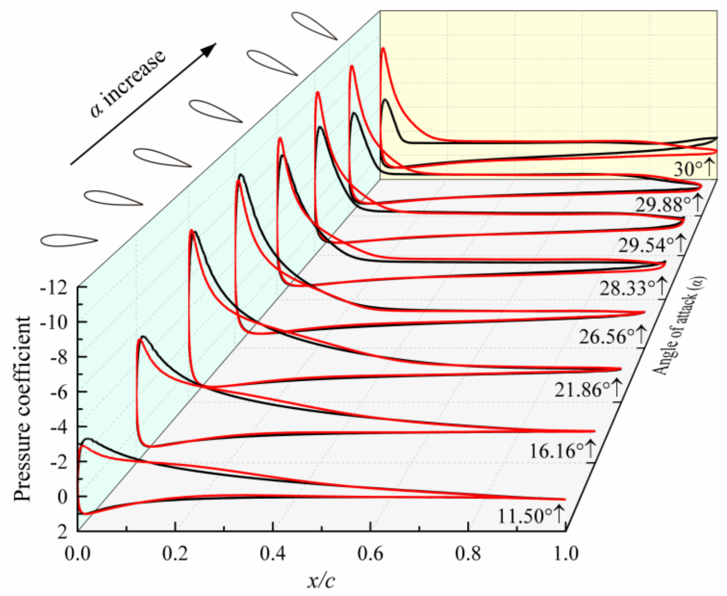

Fig 20. Comparison of pressure coefficients for NACA0018 and OPT180 in Phase 1

Due to the relatively short spanwise length of the three-dimensional blade model used in this study, the cross-section at z/c = 0.5 was selected for the comparison of velocity contours. This location effectively captures the detailed surface flow characteristics of the airfoils. Fig 21 presents the velocity contours of NACA0018 and OPT180 during Phase 1. The growth and dissipation of the high-speed region near the leading edge are clearly observed, while the forward development of the low-speed region from the trailing edge signifies the onset of a separation vortex formation. For NACA0018, the high-speed region appears closer to the blade tip. In contrast, due to the reduced leading-edge radius and increased thickness, OPT180 exhibits a broader coverage of high-speed flow near the leading edge. At α = 21.86°, both NACA0018 and OPT180 demonstrate their widest distribution of high-speed regions. As the low-speed region near the trailing edge advances toward the leading edge, it impedes the maintenance of high-speed flow at the front, causing the high-speed region to shrink progressively. At α = 29.54°, the high-speed region in NACA0018 begins to dissipate and completely disappears by α=30°. However, the modified leading-edge profile of OPT180 enhances flow attachment, resulting in only slight dissipation of the high-speed region even at large angles of attack. Furthermore, the low-speed fluid at the trailing edge of NACA0018 extends almost to the airfoil's leading edge, suppressing the accumulation of high-speed flow at the front. In contrast, OPT180 effectively suppresses the forward progression of low-speed flow from the trailing edge, contributing to its improved aerodynamic performance.

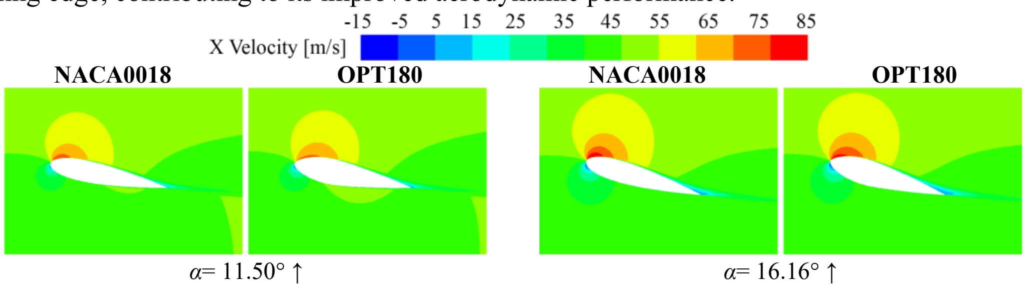

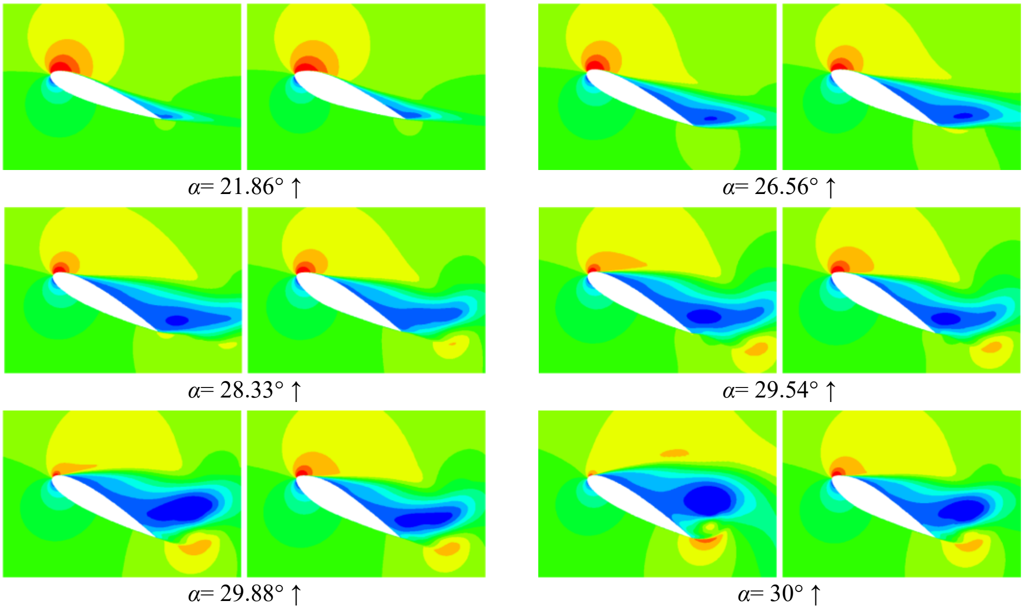

Fig 21. Comparison of velocity contours for NACA0018 and OPT180 in Phase 1

In Phase 1, the α increases from 0° to 30° over a duration of $T/3$, whereas in Phase 2, α decreases from 30° to 0° within only $T/6$. This indicates that the rate of change in α during Phase 2 is significantly faster. Fig 22 presents the C_P comparison between NACA0018 and OPT180 during Phase 2. Since the leading edge of NACA0018 had already experienced complete stall in Phase 1, it enters a deep stall condition in Phase 2, which prevents the re-establishment of high-speed flow at the leading edge. As a result, the leading-edge pressure difference remains low throughout the phase, and the aerodynamic forces do not gradually recover with the decreasing angle of attack. In contrast, OPT180 maintains a favorable leading-edge pressure difference throughout Phase 2, demonstrating superior aerodynamic performance. When $\alpha < 9.71°$, the leading-edge pressure difference of NACA0018 gradually converges with that of OPT180, indicating that at small angles of attack, the impact of airfoil shape modifications on surface pressure distribution becomes less significant.

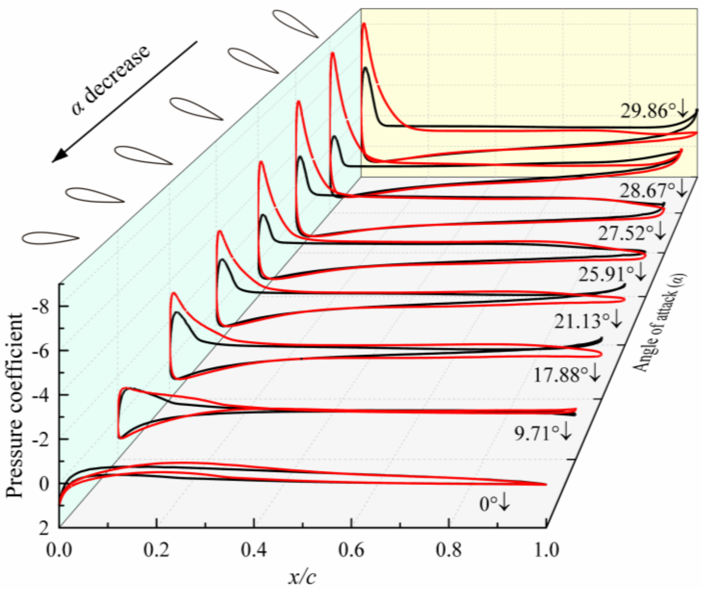

Fig 22. Comparison of pressure coefficients for NACA0018 and OPT180 in Phase 2

It is noteworthy that during Phase 2, the blade rotates about its aerodynamic center in a direction opposite to the incoming flow. This counter-rotating motion makes it more difficult for the flow to remain attached to the blade surface. Fig 23 shows the velocity contours of NACA0018 and OPT180 during Phase 2. For NACA0018, the high-speed region near the leading edge undergoes a repetitive cycle of formation and dissipation. The high-speed flow that develops at α=29.86° rapidly dissipates by α=28.67°. A similar pattern occurs at α = 27.52°, where the newly formed high-speed region also quickly vanishes, indicating that the flow struggles to remain attached to the blade surface. In contrast, OPT180 exhibits only slight diffusion of the high-speed region near the leading edge, suggesting more stable flow attachment. Additionally, NACA0018 consistently experiences strong trailing-edge flow separation, while OPT180 maintains a significantly smaller low-speed region. At α=0°, the roles of the suction and pressure surfaces are reversed, with the lower surface becoming the new suction side and beginning to accumulate high-speed flow. Compared with NACA0018, OPT180 facilitates more effective accumulation of high-speed flow on the lower surface, further demonstrating its superior aerodynamic performance.

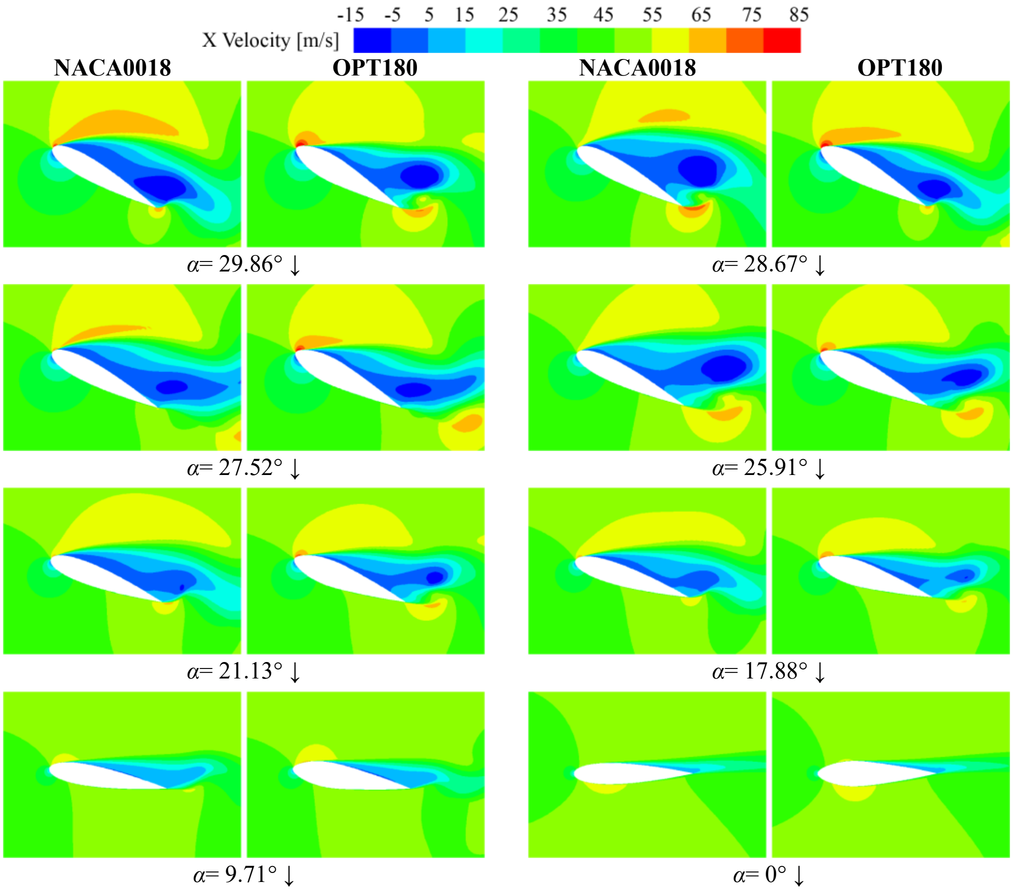

Fig 23. Comparison of velocity contours for NACA0018 and OPT180 in Phase 2

In Phase 3, the α increases from 0° to 30°, similar to Phase 1. However, the sign (±) convention in the figures only indicates the direction of blade pitching. The key difference lies in the duration: Phase 3 spans only $T/6$, which is half the time of Phase 1, indicating a much faster pitching rate. Fig 24 presents the comparison of C_P distributions between NACA0018 and OPT180 during Phase 3. It can be observed that the pressure distributions for NACA0018 at various angles of attack differ significantly from those in Phase 1. Due to the rapid variation in α, no substantial aerodynamic force loss occurs in Phase 3, suggesting that fast upstroke motion helps suppress aerodynamic degradation. As α increases during Phase 3, the leading-edge pressure difference of NACA0018 shows only a slight reduction when $\alpha > |-28.67°|$, without severe aerodynamic fluctuations. Meanwhile, OPT180 maintains a relatively large pressure difference at the leading edge even when $\alpha > |-29.87°|$, though the improvement compared to NACA0018 becomes less pronounced under such rapid upstroke conditions.

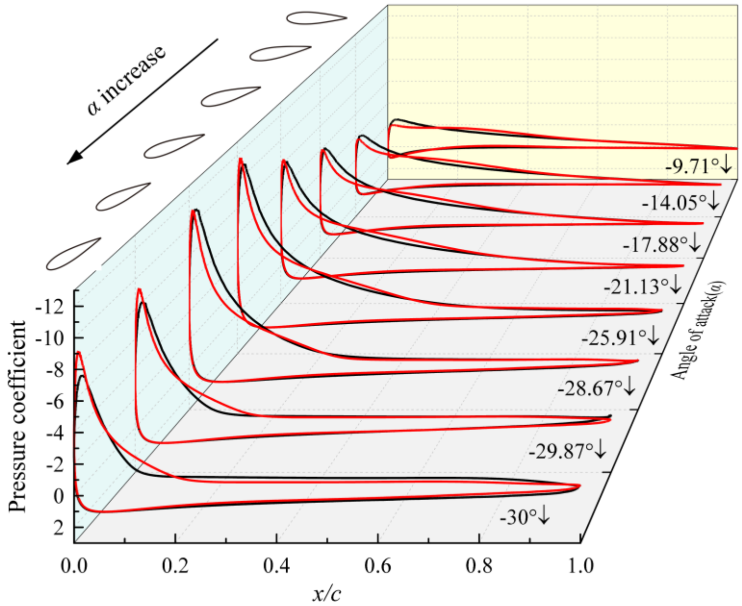

Fig 24. Comparison of pressure coefficients for NACA0018 and OPT180 in Phase 3

Fig 25 shows the velocity contours of NACA0018 and OPT180 during Phase 3. As the α increases, the extent of the high-speed region near the leading edge gradually expands. At $\alpha = |-25.91°|$, both airfoils exhibit their largest high-speed region, which corresponds to the maximum pressure difference observed in the C_P curves. When $\alpha > |-25.91°|$, the high-speed region begins to shrink due to the forward progression of trailing-edge separation vortices. However, unlike in Phase 1, the high-speed flow does not fully dissipate; instead, it remains attached to the airfoil surface. At $\alpha > |-29.87°|$, a noticeable thick layer of low-speed fluid appears near the suction-side wall of NACA0018, indicating increased flow separation. In contrast, OPT180 effectively suppresses the upstream development of trailing-edge separation vortices, keeping the low-speed fluid primarily confined to the trailing edge region.

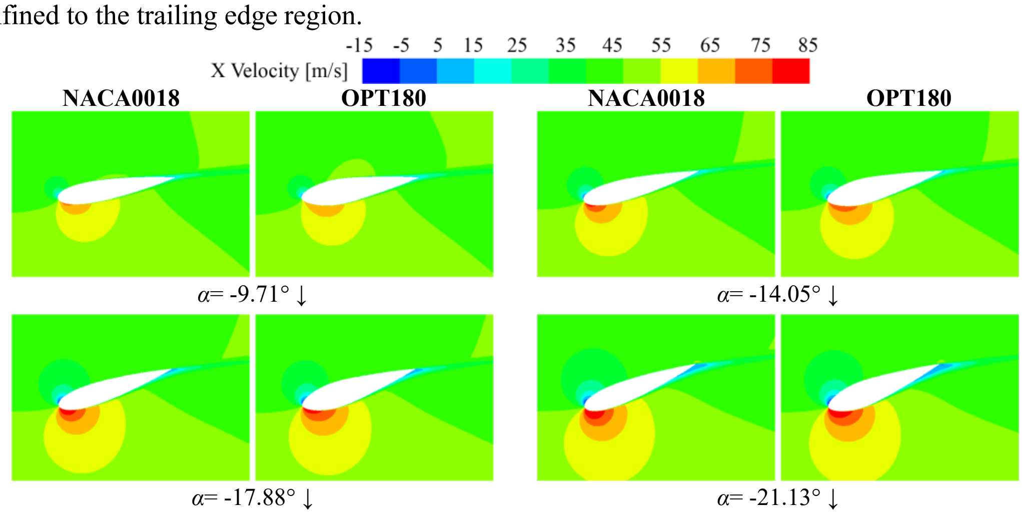

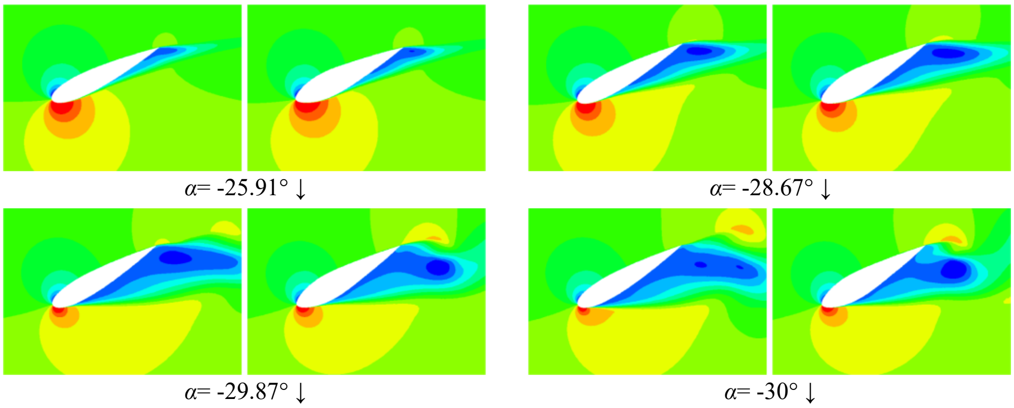

Fig 25. Comparison of velocity contours for NACA0018 and OPT180 in Phase 3

In Phase 4, the α decreases from 30° to 0°, representing a gradual downstroke process. Unlike Phase 2, where the angle of attack decreases rapidly, Phase 4 features a much slower reduction. Fig 26 presents the C_P distributions of NACA0018 and OPT180 during this phase. Although the leading-edge pressure difference of NACA0018 remained relatively stable in Phase 3, it drops sharply in Phase 4. The sudden reduction in angle of attack prevents NACA0018 from maintaining sufficient leading-edge suction. In contrast, OPT180 is largely unaffected by the gradual downstroke motion, and its optimized aerodynamic shape enables it to sustain a favorable pressure difference at the leading edge. Notably, when α = |-27.51°|, the leading-edge pressure difference of OPT180 is approximately three times that of NACA0018, indicating a significant improvement in aerodynamic performance. As α continues to decrease and becomes less than |-11.5°|, the pressure differences at the leading edge for both airfoils converge. This is because, at low angles of attack, the surface flow remains fully attached for both geometries.

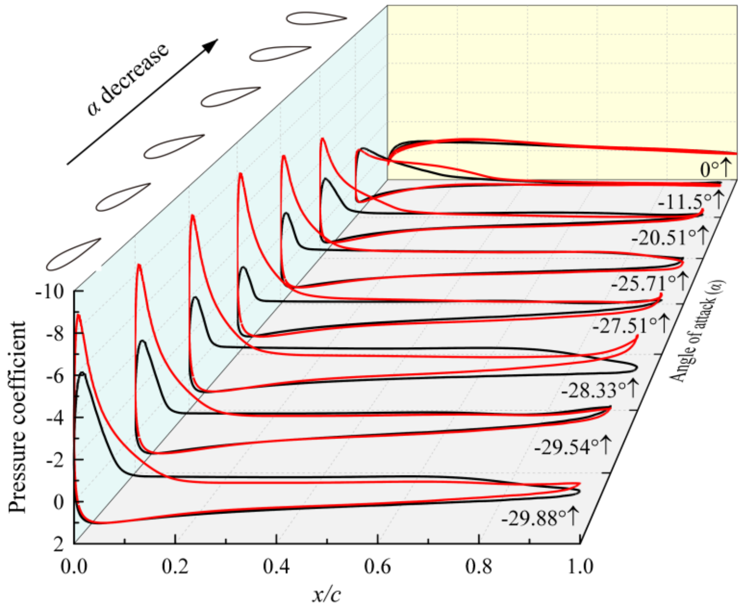

Fig 26. Comparison of pressure coefficients for NACA0018 and OPT180 in Phase 4

Fig 27 shows the velocity contours of NACA0018 and OPT180 during Phase 4. During the downstroke process, dynamic stall is more likely to occur, as the blade's rotational motion is opposite to the incoming flow, resulting in unstable surface flow conditions. For NACA0018, the high-speed region near the leading edge rapidly diffuses and then vanishes, indicating that the high-speed flow cannot remain attached to the suction-side leading edge. In contrast, OPT180 maintains a stable high-speed region near the leading edge, with only minor diffusion, demonstrating better flow attachment. The forward progression of the low-speed region from the trailing edge in NACA0018 plays a critical role in the rapid dissipation of the high-speed flow. At $\alpha < |-28.33°|$, the size of the low-speed region near the trailing edge in OPT180 is approximately half that of NACA0018. The optimized aerodynamic shape of OPT180 effectively suppresses flow separation and significantly improves the aerodynamic performance of the blade.

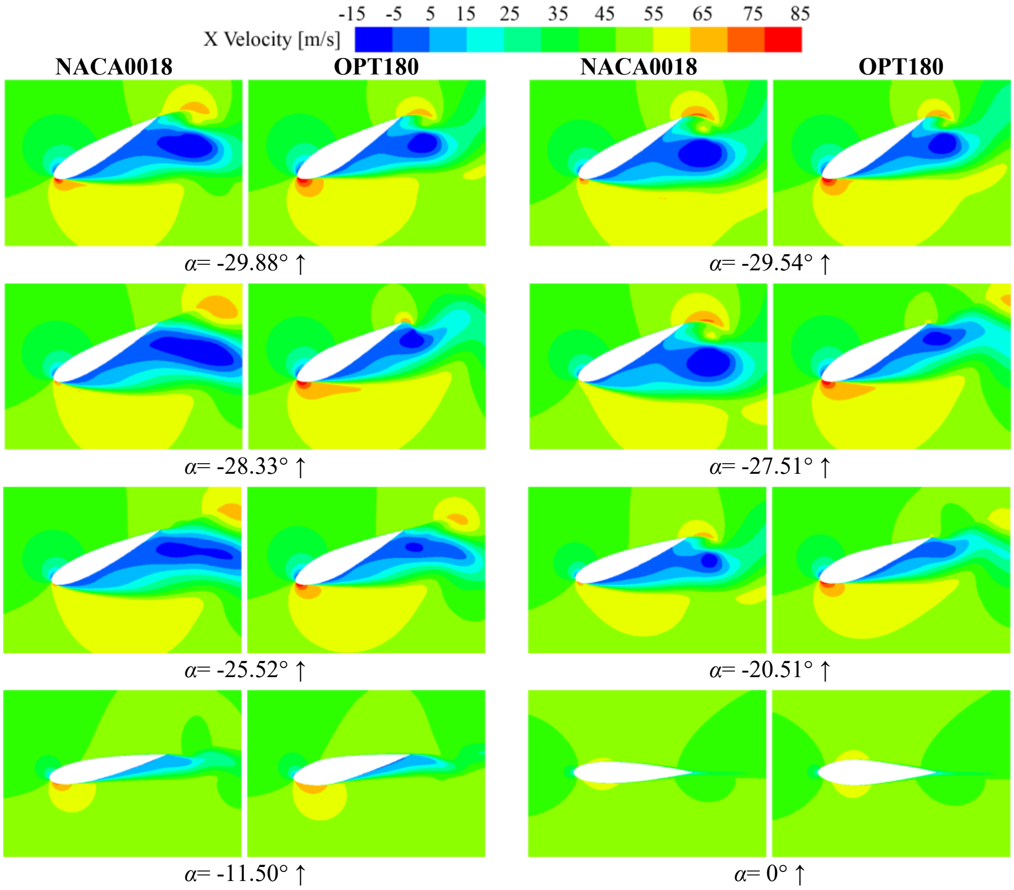

Fig 27. Comparison of velocity contours for NACA0018 and OPT180 in Phase 4

In summary, for the baseline airfoil NACA0018, a comparison between Phases 1 and 3 (both involving an increase in angle of attack from 0° to 30°) reveals a significant difference in aerodynamic behavior. In Phase 1, where the angle increases gradually, severe leading-edge dynamic stall occurs. In contrast, in Phase 3, with a rapid increase in angle of attack, no leading-edge stall is observed; instead, only trailing-edge separation vortices are present. When comparing the downstroke phases (Phases 2 and 4), where the angle of attack decreases from 30° to 0°, NACA0018 consistently exhibits rapid dissipation of the leading-edge high-speed region, resulting in poor aerodynamic performance across both phases. The optimized airfoil OPT180, by contrast, demonstrates enhanced aerodynamic performance throughout all four phases, maintaining a higher leading-edge pressure difference. The aerodynamic shape modifications effectively preserve the high-speed flow near the leading edge while suppressing the forward propagation of trailing-edge separation vortices. This reduces flow separation and improves dynamic stall characteristics. Notably, in Phases 2 and 4 where the leading-edge high-speed region in NACA0018 completely vanishes, the OPT180 successfully retains a stable high-speed region near the leading edge. This ability to sustain attached flow under adverse conditions is the key factor behind the significantly improved aerodynamic performance of the OPT180 airfoil.

5.4. Flow structure of Q criterion

The Q-criterion is a vortex identification method based on the velocity gradient tensor, suitable for extracting three-dimensional vortex cores in flow fields. A positive Q value (Q > 0) indicates that the local rotational strength (vorticity) dominates over the strain rate (shear or stretching), making it an effective tool for identifying vortex shedding phenomena during dynamic stall. Hunt et al. [115] decomposed the velocity gradient tensor into a symmetric tensor $\boldsymbol{X}$ and an antisymmetric tensor $\boldsymbol{Y}$, which can be expressed by Cauchy-Stokes decomposition as follows:

$$Q=\frac{1}{2}\left(\|\boldsymbol{X}\|_F^2-\|\boldsymbol{Y}\|_F^2\right) \tag{34}$$

where $\|\square\|_F^2$ is the Frobenius norm of the matrix; Q is the second invariant of the velocity tensor.

Since vortex shedding primarily occurs at high angles of attack, Q-criterion isosurfaces for NACA0018 and OPT180 at large angles of attack are presented, as shown in Fig 28. The SST k–ω turbulence model is employed to capture the dominant large-scale vortex structures, enabling the identification of vortex core clustering and shedding. Due to the high angle of attack, both NACA0018 and OPT180 generate large-scale vortical structures.

In Phase 1, as the angle of attack increases, the vortex on the surface of NACA0018 continues to grow. However, due to the modified aerodynamic shape, the surface vortex on OPT180 is fragmented into smaller scale structures, which prevents the continuous growth of large vortices and reduces energy loss. As a result, the vortex core size is reduced at α = 29.88°. In Phase 2, although the angle of attack decreases, the vortex structure on NACA0018 changes only slightly. In contrast, the vortex on OPT180 is significantly weakened, with its size reduced by nearly half at α = 25.91°. Additionally, the leading-edge separation point moves downstream. In Phase 3, although the blade is still pitching downward, the angle of attack increases. Similar to Phase 1, as α increases from |−28.67°| to |−30°|, larger and more chaotic vortices are observed on the surface of NACA0018. In comparison, vortex growth is effectively suppressed on OPT180. In Phase 4, as the angle of attack decreases, the wake vortices of OPT180 dissipate more rapidly, and its leading-edge separation point moves further downstream than that of NACA0018, especially at α = −25.52°. This indicates that the aerodynamic shape optimization effectively delays flow separation and suppresses vortex core development.

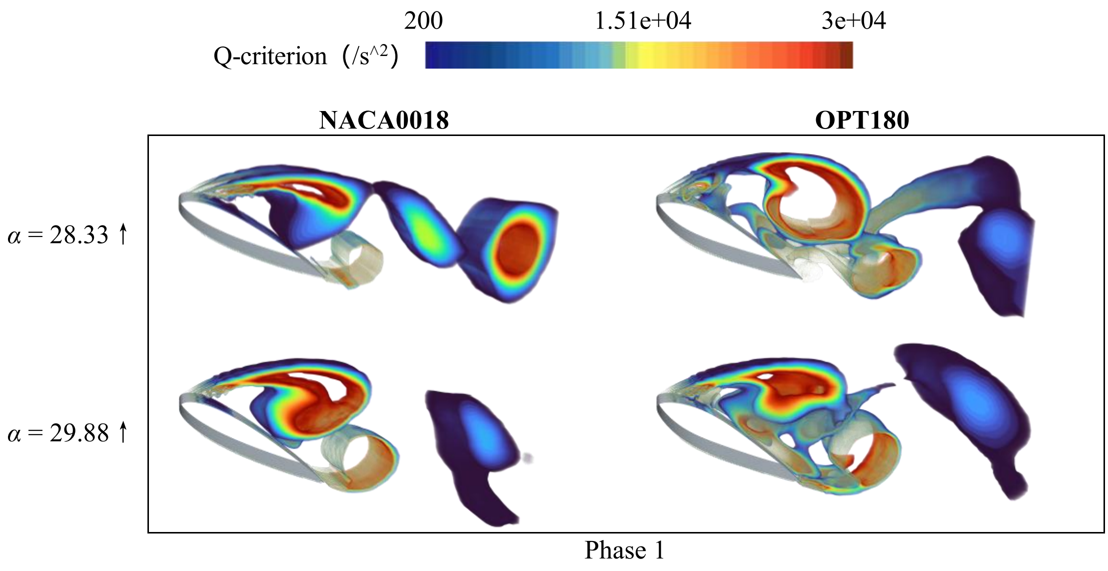

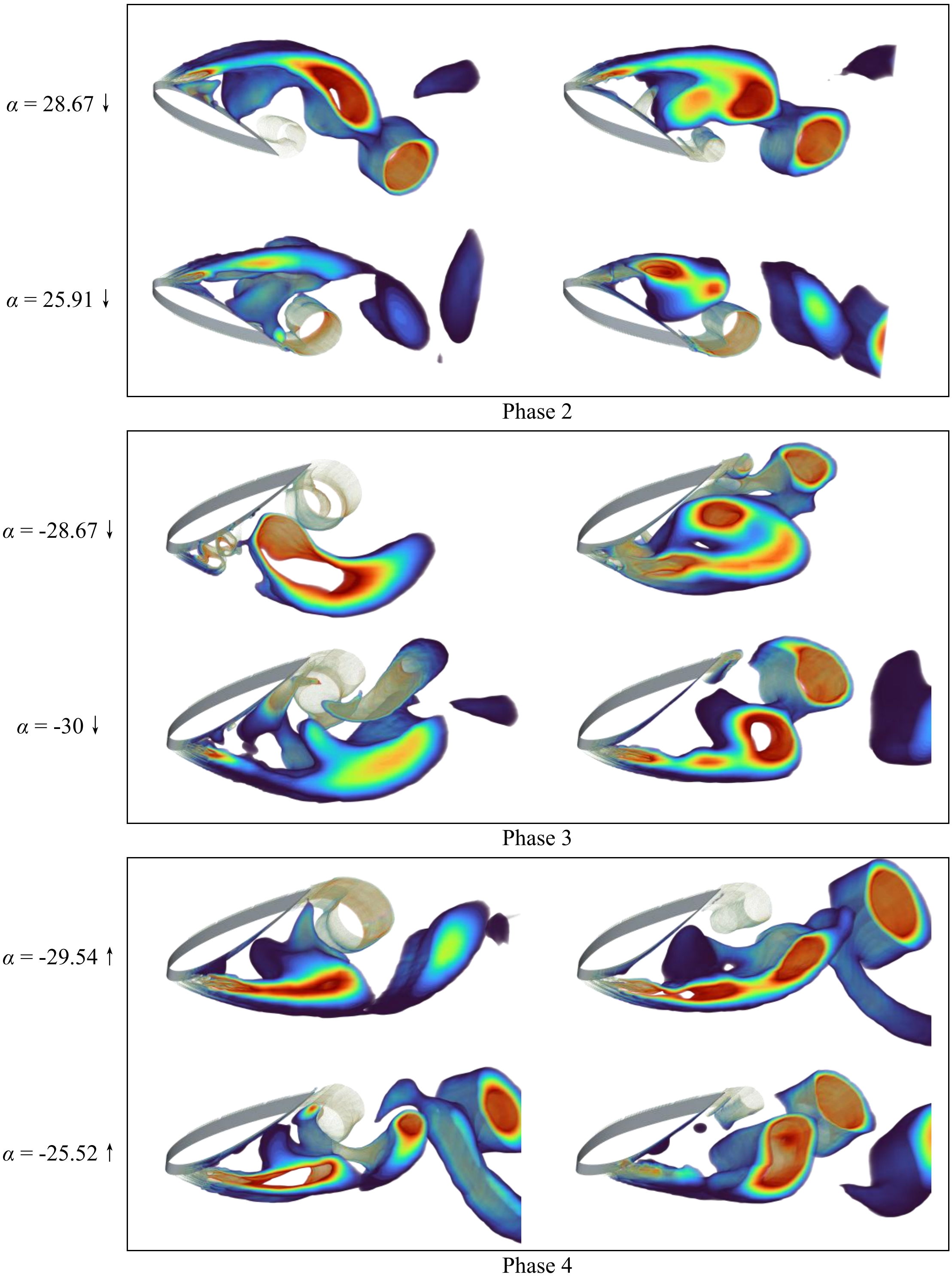

Fig 28. Distribution of the Q isosurface at various angles of attack.

6. Conclusion

This study investigates the dynamic stall phenomenon induced by the unique Darrieus-type pitching motion (DPM) of VAWT blades, with the aim of improving aerodynamic performance. A data-driven aerodynamic shape optimization (ASO) approach based on a GPR surrogate model is proposed, and a global optimization algorithm is employed to optimize the baseline NACA0018 airfoil. The dynamic stall characteristics and flow field structures of the baseline and optimized airfoils are comparatively analyzed. The main conclusions are as follows:

(1) Compared with NACA0018, the optimized airfoil (OPT180) exhibits a reduced leading-edge radius, increased thickness, and a rearward shift of the maximum thickness position. The curvature variation is most pronounced at the location of maximum thickness. For dynamic stall induced by DPM, the maximum thickness and surface curvature are identified as key factors influencing aerodynamic characteristics.

(2) The mean drag and moment coefficients of OPT180 are reduced by 18.28% and 12.23%, respectively. Although the maximum lift coefficient decreases, the mean lift coefficient increases, effectively reducing aerodynamic losses in the stall region. As the tangential force coefficient contributes to the torque generation in VAWTs, the 23.87% increase observed in OPT180 indicates not only the suppression of negative torque but also a reduction in peak torque, resulting in a more stable torque output from the blade.

(3) Under DPM, Phases 1 and 2 correspond to a slow increase and rapid decrease in angle of attack. During these Phases, NACA0018 exhibits not only diffusion in the high-speed region near the leading edge but also a large region of reverse flow near the trailing edge. Phases 3 and 4 correspond to a rapid increase and slow decrease in angle of attack. Although NACA0018 does not experience leading-edge stall in Phase 3, the high-speed region dissipates rapidly in Phase 4. These results indicate that a slower rate of change in angle of attack is more likely to induce dynamic stall.

(4) OPT180 demonstrates superior aerodynamic performance across all four phases. The high-speed region near the leading edge exhibits only a slight reduction and consistently maintains a higher pressure difference at the leading edge. The modified aerodynamic shape effectively sustains high-speed flow near the leading edge while suppressing the upstream propagation of low-speed flow from the trailing edge. This reduces flow separation and thereby improves the dynamic stall characteristics.

(5) Vortex structures in the flow were analyzed using the Q-criterion. For NACA0018, larger and more chaotic vortex cores develop across the surface with varying angles of attack. In contrast, the increased curvature at the maximum thickness location of OPT180 suppresses the continuous growth of vortex structures at high angles of attack, preventing excessive energy loss. Moreover, the trailing-edge vortices dissipate more rapidly, and the leading-edge separation point shifts downstream, further enhancing aerodynamic performance.

Acknowledgments

The authors would like to acknowledge the support of National Key Research and Development Program of China (grand No. 2024YFA1012501) and National Natural Science Foundation of China (grand No. 52476212 and 52376204). Shanghai Science and Technology Development Foundation (grand No. 24ZR1454800), and State Key Laboratory of Mechanical System and Vibration [China, No. MSV202411], and Innovate UK (10161107) for "Smart Renewable Energy Generation and Storage System for Sustainable Power (SMARTPOWER)” project, and funded by the China Scholarship Council.

Reference

[1] Roga S, Bardhan S, Kumar Y, et al. Recent technology and challenges of wind energy generation: A review[J]. Sustainable Energy Technologies and Assessments, 2022, 52:102239.

[2] Smirnova E, Kot S, Kolpak E, et al. Governmental support and renewable energy production: A cross-country review[J]. Energy, 2021, 230:120903.

[3] Tumse S, Bilgili M, Yildirim A, et al. Comparative Analysis of Global Onshore and Offshore Wind Energy Characteristics and Potentials[J]. Sustainability, 2024, 16(15):6614.

[4] Global Wind Energy Council. Global wind report 2025[J]. 2025, London, United Kingdom.

[5] Eftekhari H, Al-Obaidi AS, Eftekhari S. Aerodynamic performance of vertical and horizontal axis wind turbines: A comparison review[J]. Indonesian Journal of Science and Technology, 2022, 7(1):65-88.

[6] Rawajfeh MA, Gomaa MR. Comparison between horizontal and vertical axis wind turbine[J]. International Journal of Applied Power Engineering, 2023, 12(1):13-23.

[7] Santamaría L, Oro JM, Díaz KM, et al. Novel methodology for performance characterization of vertical axis wind turbines (VAWT) prototypes through active driving mode[J]. Energy Conversion and Management, 2022, 258:115530.

[8] Aravindhan N, Natarajan MP, Ponnuvel S, Devan PK. Recent developments and issues of small-scale wind turbines in urban residential buildings-A review[J]. Energy & Environment, 2023, 34(4):1142-69.

[9] Tjiu W, Marnoto T, Mat S, Ruslan MH, Sopian K. Darrieus vertical axis wind turbine for power generation II: Challenges in HAWT and the opportunity of multi-megawatt Darrieus VAWT development. Renewable Energy. 2015 Mar 1;75:560-71.

[10] Sedaghat A, Mirhosseini M, Moghimi Zand M. Aerodynamic design and economical evaluation of site specific horizontal axis wind turbine (HAWT). Energy Equipment and Systems. 2014 Jan 1;2(1):43-56.

[11] Mohan Kumar P, Sivalingam K, Lim TC, Ramakrishna S, Wei H. Review on the evolution of Darrieus vertical axis wind turbine: Large wind turbines. Clean technologies. 2019 Aug 7;1(1):205-23.

[12] Seifi Davari H, Seify Davari M, Botez RM, Chowdhury H. Advancements in vertical axis wind turbine technologies: A comprehensive review. Arabian Journal for Science and Engineering. 2025 Feb;50(4):2169-216.

[13] Ghasemian M, Ashrafi ZN, Sedaghat A. A review on computational fluid dynamic simulation techniques for Darrieus vertical axis wind turbines. Energy Conversion and Management. 2017 Oct 1;149:87-100.

[14] Gupta A, Ait Abderrahmane H, Janajreh I. Flow analysis and sensitivity study of vertical-axis wind turbine under variable pitching. Applied Energy. 2024 Mar 15;358:122648.

[15] Li C, Xiao Y, Xu YL, Peng YX, Hu G, Zhu S. Optimization of blade pitch in H-rotor vertical axis wind turbines through computational fluid dynamics simulations. Applied Energy. 2018 Feb 15;212:1107-25.

[16] Radhakrishnan J, Sridhar S, Zuber M, Ng EY, Shenoy S. Design optimization of a Contra-Rotating VAWT: A comprehensive study using Taguchi method and CFD. Energy Conversion and Management. 2023 Dec 15;298:117766.

[17] Wang Z, Wang Y, Zhuang M. Improvement of the aerodynamic performance of vertical axis wind turbines with leading-edge serrations and helical blades using CFD and Taguchi method. Energy conversion and management. 2018 Dec 1;177:107-21.

[18] Sobhani E, Ghaffari M, Maghrebi MJ. Numerical investigation of dimple effects on darrieus vertical axis wind turbine. Energy. 2017 Aug 15;133:231-41.

[19] Bhavsar H, Roy S, Niyas H. Aerodynamic performance enhancement of the DU99W405 airfoil for horizontal axis wind turbines using slotted airfoil configuration. Energy. 2023 Jan 15;263:125666.

[20] Liu Q, Miao W, Ye Q, Li C. Performance assessment of an innovative Gurney flap for straight-bladed vertical axis wind turbine. Renewable Energy. 2022 Feb 1;185:1124-38.

[21] Hao W, Bashir M, Li C, Sun C. Flow control for high-solidity vertical axis wind turbine based on adaptive flap. Energy conversion and management. 2021 Dec 1;249:114845.

[22] Yin Y, Zong H, Wu Y, Li J, Liang H. Improving the power production of a vertical axis wind turbine by intelligent closed-loop control of synthetic jet actuators. Energy. 2025 Jun 1;324:135988.

[23] Sun J, Huang D. Numerical investigation of boundary layer suction control positions on airfoils for vertical-axis wind turbine. Journal of Mechanical Science and Technology. 2021 Jul;35:2903-14.

[24] Cai X, Zhang Y, Ding W, Bian S. The aerodynamic performance of H-type darrieus VAWT rotor with and without winglets: CFD simulations. Energy Sources, Part A: Recovery, Utilization, and Environmental Effects. 2024 Dec 31;46(1):2625-36.

[25] Chong WT, Fazlizan A, Poh SC, Pan KC, Hew WP, Hsiao FB. The design, simulation and testing of an urban vertical axis wind turbine with the omni-direction-guide-vane. Applied Energy. 2013 Dec 1;112:601-9.

[26] Wong KH, Chong WT, Poh SC, Shiah YC, Sukiman NL, Wang CT. 3D CFD simulation and parametric study of a flat plate deflector for vertical axis wind turbine. Renewable energy. 2018 Dec 1;129:32-55.

[29] Abd Aziz PD, Mohamad AR, Hamidon FZ, Mohamad N, Salleh N, Yunus NM. A simulation study on airfoils using VAWT design for low wind speed application. In2014 4th International Conference on Engineering Technology and Technopreneuship (ICE2T) 2014 Aug 27 (pp. 105-109). IEEE.

[30] Mitchell S, Ogbonna I, Volkov K. Aerodynamic characteristics of a single airfoil for vertical axis wind turbine blades and performance prediction of wind turbines. Fluids. 2021 Jul 13;6(7):257.

[31] Wang Q, Liu B, Hu C, Wang F, Yang S. Aerodynamic shape optimization of H-VAWT blade airfoils considering a wide range of angles of attack. International Journal of Low-Carbon Technologies. 2022;17:147-59.

[32] Zhang R, Li D, Chang H, Wei X, Wang H. Multi-objective optimization on blade airfoil of vertical axis wind turbine. Physics of Fluids. 2024 Aug 1;36(8).

[33] Hicks RM, Murman EM, Vanderplaats GN. An assessment of airfoil design by numerical optimization. 1974, No. A-5506.

[34] Wang K, Han Z, Zhang K, Song W. Efficient Global Aerodynamic Shape Optimization of a Full Aircraft Configuration Considering Trimming. Aerospace. 2023 Aug 21;10(8):734.

[35] Liu J, Chen R, Lou J, Hu Y, You Y. Deep-learning-based aerodynamic shape optimization of rotor airfoils to suppress dynamic stall. Aerospace Science and Technology. 2023 Feb 1;133:108089.

[36] Izci D, Ekinci S. A novel hybrid ASO-NM algorithm and its application to automobile cruise control system. InProceedings of 2nd International Conference on Artificial Intelligence: Advances and Applications: ICAIAA 2021 2022 Feb 14 (pp. 333-343). Singapore: Springer Nature Singapore.

[39] Boudis A, Hamane D, Guerri O, Bayeul-Lainé AC. Airfoil shape optimization of a horizontal axis wind turbine blade using a discrete adjoint solver. Journal of Applied Fluid Mechanics. 2023 Apr 1;16(4):724-38.

[40] Li J, Dao MH, Le QT. Data-driven modal parameterization for robust aerodynamic shape optimization of wind turbine blades. Renewable Energy. 2024 Apr 1;224:120115.

[41] Duan Y, Fan Z, Wu W, Chen T. Study on global aerodynamic shape optimization of transonic compressor blade. International Journal of Turbo & Jet-Engines. 2022 Aug 1;39(3):251-63.

[42] Liang C, Li H. Aerofoil optimization for improving the power performance of a vertical axis wind turbine using multiple streamtube model and genetic algorithm. Royal Society Open Science. 2018 Jul 25;5(7):180540.

[43] Sanaye S, Hosseinkhani A. Innovative multiobjective optimization of a curved-blade vertical axis wind turbine modeled by modified double multiple streamtube method. Energy Science & Engineering. 2024 May;12(5):2118-36.

[44] Zhao Z, Yan C, Wang T, Xu B, Zheng Y. Study on approach of performance improvement of VAWT employing double multiple stream tubes model. Journal of Renewable and Sustainable Energy. 2017 Mar 1;9(2).

[45] Chern MJ, Goytom Tewolde D, Kao CC, Vaziri N. Vertical-axis wind turbine blade-shape optimization using a genetic algorithm and direct-forcing immersed boundary method. Journal of Energy Engineering. 2021 Apr 1;147(2):04020091.

[46] Chen Y, Hord K, Prater R, Lian Y, Bai L. Design optimization of a vertical axis wind turbine using a genetic algorithm and surrogate models. In12th AIAA Aviation Technology, Integration, and Operations (ATIO) Conference and 14th AIAA/ISSMO Multidisciplinary Analysis and Optimization Conference 2012 (p. 5434).

[47] Sanaye S, Rezaeian P, Farvizi A. A novel surrogated approach for optimizing a vertical axis wind turbine with straight blades. Wind Energy. 2024 Sep;27(9):953-74.

[48] Cardoso Netto D, Ramirez Gustavo R, Manzanares Filho N. Surrogate-based design optimization of a h-darrieus wind turbine comparing classical response surface, artificial neural networks, and kriging. Journal of Applied Fluid Mechanics. 2023 Apr 1;16(4):703-16.

[49] Wang Q, Zhang Z. Airfoil Optimization Design of Vertical-Axis Wind Turbine Based on Kriging Surrogate Model and MIGA. Energies. 2025 Jun 3;18(11):2927.

[50] Cheng B, Yao Y. Machine learning based surrogate model to analyze wind tunnel experiment data of Darrieus wind turbines. Energy. 2023 Sep 1;278:127940.

[51] Dorosti E, Shabani A, Vijayaraghavan K. Efficiency-Driven Supervised Learning Regressors in Power Modeling and Optimization of Vertical Axis Wind Turbines. InEnergy Sustainability 2024 Jul 15 (Vol. 87899, p. V001T01A003). American Society of Mechanical Engineers.

[52] Wang S, Ingham DB, Ma L, Pourkashanian M, Tao Z. Numerical investigations on dynamic stall of low Reynolds number flow around oscillating airfoils. Computers & fluids. 2010 Oct 1;39(9):1529-41.

[53] Li QA, Maeda T, Kamada Y, Murata J, Furukawa K, Yamamoto M. Effect of number of blades on aerodynamic forces on a straight-bladed Vertical Axis Wind Turbine. Energy. 2015 Oct 1;90:784-95.

[54] Allet A, Paraschivoiu I. Numerical simulation of dynamic stall around an airfoil in Darrieus motion. Journal of solar energy engineering. 1999, 121(1): 69-76.

[55] Hand B, Kelly G, Cashman A. Numerical simulation of a vertical axis wind turbine airfoil experiencing dynamic stall at high Reynolds numbers[J]. Computers & Fluids, 2017, 149: 12-30.

[56] Karolczuk A, Kurek M. Fatigue life uncertainty prediction using the Monte Carlo and Latin hypercube sampling techniques under uniaxial and multiaxial cyclic loading[J]. International Journal of Fatigue, 2022, 160: 106867.

[57] Rajabi M M , Ataie-Ashtiani B , Janssen H . Efficiency enhancement of optimized Latin hypercube sampling strategies: Application to Monte Carlo uncertainty analysis and meta-modeling[J]. Advances in Water Resources, 2015, 76(Feb.):127-139.

[58] Liu Y, Xue Y, Chen Y, et al. Identification of nonparametric thermodynamic model and optimization of ocean thermal energy conversion radial inflow turbine[J]. Applied Energy, 2022, 321: 119348.

[61] Gu L, Yang R J. On reliability-based optimisation methods for automotive structures[J]. International Journal of Materials and Product Technology, 2006, 25(1-3): 3-26.

[62] Shi L, Yang R J, Zhu P. A method for selecting surrogate models in crashworthiness optimization[J]. Structural and Multidisciplinary Optimization, 2012, 46: 159-170.

[63] Schulz E, Speekenbrink M, Krause A. A tutorial on Gaussian process regression: Modelling, exploring, and exploiting functions[J]. Journal of Mathematical Psychology, 2018, 85: 1-16.

[64] Shi J Q, Choi T. Gaussian process regression analysis for functional data[M]. CRC press, 2011.

[65] Lázaro-Gredilla M, Quinonero-Candela J, Rasmussen C E, et al. Sparse spectrum Gaussian process regression[J]. The Journal of Machine Learning Research, 2010, 11: 1865-1881.

[66] Jones D R, Schonlau M, Welch W J. Global optimization of expensive black-box functions[J]. Journal of Global Optimization, 1998, 13(4): 455-492.

[67] Sobester A, Forrester A, Keane A. Engineering design via surrogate modelling: a practical guide[M]. John Wiley & Sons, 2008.

[68] Storn R, Price K. Differential evolution-a simple and efficient heuristic for global optimization over continuous spaces[J]. Journal of global optimization, 1997, 11(4): 341.

[69] Wickens R H. Wind tunnel investigation of dynamic stall of a NACA 0018 Airfoil oscillating in Pitch[J]. National Aeronautical Establishment, Aeronautical Note NAE-AN-27, NRC no 24262, 1985.

[70] Strickland JM, Stevens RJ. Effect of thrust coefficient on the flow blockage effects in closely-spaced spanwise-infinite turbine arrays. InJournal of Physics: Conference Series, 1618 (6): 062069.